



ACAT1 Fan Stage Broadband Noise Prediction Using Large-Eddy Simulation and Analytical Models

Danny Lewis,* Stéphane Moreau,† and Marc C. Jacob‡

Laboratoire de Mécanique des Fluides et d'Acoustique, Université de Lyon, CNRS, Institut National des Sciences Appliquées de Lyon, Université Claude Bernard Lyon I, UMR 5509, F-69134 Ecully, France

and

Marlène Sanjosé§

École de Technologie Supérieure, Montréal, QC H3C1K3, Canada

<https://doi.org/10.2514/1.J060163>

The present paper deals with the assessment of the turbulent flow through and the noise radiation of the ACAT1 fan stage, which was tested in the framework of the European project TurbonoiseBB. It aims at analyzing and predicting the broadband noise resulting from the impact of the fan wakes onto the outlet guide vane (OGV) at approach condition. This is achieved via a large-eddy simulation (LES) of the full fan-OGV stage that is in good agreement with the mean flow measurements. Some disparities regarding the turbulent content of the flow are, however, highlighted. The main flow features and the broadband noise sources are examined. The noise is then estimated using two different hybrid approaches: LES-informed analytical models, using Hanson's and Posson's cascade models, and a numerical approach coupling the LES with the free-field Ffowcs Williams and Hawkings (FW-H) analogy, and Goldstein's in-duct acoustic analogy. The shape of the noise spectra provided by the analytical models is relatively similar to that of the sound measurements, whereas some discrepancies on the absolute noise levels may appear depending on the analytical model and the turbulence length scale estimate. The numerical approach reveals that accounting for the duct effect through Goldstein's analogy provides noise levels much closer to the measurements than those obtained with the free-field analogy, which significantly overestimates the broadband noise. Both the analytical and the numerical approaches suggest that additional significant noise sources might be present in both the experiment and the simulation.

Nomenclature

Subscripts

c	=	autocorrelation-based estimate (integral length scale)
j	=	Jurdic estimate (integral length scale)
p	=	Pope estimate (integral length scale)
rms	=	root mean square

Superscript

$'$	=	variable fluctuations
-----	---	-----------------------

I. Introduction

THE fan-outlet guide vane (fan-OGV) stage of aircraft engines is currently being considered as one of the major contributors to the total noise radiated by an aircraft, particularly at approach and takeoff operating conditions. This trend will intensify with the future ultra high-bypass-ratio (UHBR) engine architecture, which will be characterized by an increased bypass ratio resulting from a larger diameter. To meet the increasingly stringent noise regulation require-

ments, significant progress has already been achieved by aircraft manufacturers. Most of them are related to the tonal component of the fan-OGV stage noise, which has been reduced thanks to an intensive use of acoustic liners and a smart blade/vane count selection exploiting the duct cutoff properties. However, little progress has been made in reducing the broadband component of the noise. It originates from stochastic phenomena involving the interaction of turbulent structures with solid surfaces such as walls, blades, and vanes. The main mechanism responsible for both broadband and tonal noise generation is the rotor–stator interaction (RSI), which consists in the impingement of the rotor turbulent wakes onto the stator, generating an unsteady loading on the vanes. Additionally, in a near future this mechanism will be all the more dominant because the fan-OGV spacing in UHBR engines will be reduced for the sake of engine performance. This mechanism has been extensively studied over the past few years, using multiple approaches, which are gathered in Moreau [1], Moreau and Roger [2], and Peake and Parry [3].

To bypass the prohibitive CPU cost of direct numerical simulations, hybrid methods have been developed to carry out studies on the RSI mechanism at a more reasonable cost. These methods are generally a two-step process that separates the computation of the acoustic sources from the propagation. The present paper focuses on the two following hybrid approaches:

1) *Semi-analytical approach*: This method couples a computational fluid dynamics (CFD) computation with an analytical model. The flow parameters that characterize the impinging flow are extracted from the CFD simulation to feed the analytical model that computes the resulting unsteady loading. The latter is then considered as an equivalent dipole source distribution in an acoustic analogy in order to compute the associated radiated noise [4–6]. This approach only requires flow simulations using statistical turbulence models (Reynolds-averaged Navier–Stokes (RANS), unsteady RANS (URANS)), making it possible to compute the RSI noise at an affordable cost especially in an industrial context. Nevertheless, the inherent assumptions made in the turbulence models and the necessary geometry simplifications of the models induce a loss of accuracy. These models may also be applied to mean flow data extracted from high-fidelity unsteady simulations

Presented as Paper 2020-2519 at the AIAA Aviation 2020 Forum, Virtual Event, June 15–19, 2020; received 9 September 2020; revision received 17 May 2021; accepted for publication 18 May 2021; published online 30 July 2021. Copyright © 2021 by the authors. Published by the American Institute of Aeronautics and Astronautics, Inc., with permission. All requests for copying and permission to reprint should be submitted to CCC at www.copyright.com; employ the eISSN 1533-385X to initiate your request. See also AIAA Rights and Permissions www.aiaa.org/randp.

*Post-Doctoral Fellow, Ecole Centrale de Lyon, 36 avenue Guy de Collongue, F-69134 Ecully Cedex, France; danny.lewis@ec-lyon.fr.

†Professor, Mechanical Engineering Department, Groupe d'Acoustique de l'Université de Sherbrooke.

‡Professor, Ecole Centrale de Lyon, 36 avenue Guy de Collongue, F-69134 Ecully Cedex, France. Member AIAA.

§Professor, Department of Mechanical Engineering.

(such as large-eddy simulation (LES)), for comparison purposes, although such unsteady simulations are not meant to feed statistical models in the first place. The semi-analytical approach has been extensively used to estimate the broadband RSI noise, notably by Leonard et al. [4], Posson et al. [7], Grace et al. [8], Grace [9], Grace et al. [10], Kissner et al. [11], Guerin et al. [12,13], Polacsek et al. [14], Nallasamy and Envia [15], Jurdic et al. [16], and Masson et al. [6].

2) *Numerical approach* [4]: This method couples a fully unsteady flow computation, an LES in the present study, with an acoustic analogy such as the Ffowcs Williams and Hawkings (FW-H) [17] free-field analogy, or the Goldstein [18] duct analogy to recover the acoustic far field. These flow simulations enable a direct computation of the unsteady loading on the vane, the accuracy of which is set by the mesh itself. The main drawback of such hybrid approaches is that the Green's function is only known for canonical cases (free-field, uniform flow, annular cylindrical ducts, with possible but complex extensions to slowly varying ducts, lined ducts, mean swirling flows). As a consequence, some specific features are inevitably neglected in the wave propagation, with a possible impact on the accuracy of the method. Shear flows are also usually neglected as their effects are expected to be rather low compared with first-order accuracy when using infinite annular duct/uniform flow Green's function. Such a numerical approach has been successfully applied to fan noise predictions by Leonard et al. [4], Pérez Arroyo et al. [19], and Polacsek et al. [14]. A different hybrid approach relying on the use of the porous formulation of the FW-H analogy was also investigated by Gonzalez-Martino and Casalino [20] and Casalino et al. [21,22] (see Moreau's review [23] for a comprehensive description of the available methods). Such an approach has not been investigated in the present study because it requires an accurate prediction of the acoustic near-field that would have led to a significant increase in the computational cost of the simulation.

The objective of the present paper is to assess the capacity of the two aforementioned methods to carry out reliable predictions of the broadband RSI noise. It proposes an analysis of the coupling of LES with both analytical models and acoustic analogies. This study is an alternative to the work previously performed by Lewis et al. [24], which focused on RANS-informed analytical models only. The LES as well as the broadband noise predictions have all been performed on the ACAT1 configuration tested in 2018 in the AneCom UFFA facility in Wildau (Germany) in the framework of the European project TurbonoiseBB [25–28]. An in-depth analysis of the flow physics is conducted in order to assess the turbulent flow

characteristics related to the RSI mechanism and to assess the validity of some assumptions made within the analytical models.

II. Turbofan Configuration

The ACAT1 turbofan model consists of 20 fan blades and 44 stator vanes. Two configurations have been tested: one with a short fan-OGV gap and an additional one with a longer rotor–stator gap. Figure 1 displays these two configurations along with the measuring instruments for both the acoustic and the aerodynamic measurements. Ring arrays were used for the acoustic measurements at the inlet (CMD1), interstage (ISTG), and bypass (CMD3) sections, and axial arrays at the interstage and in the bypass duct. Moreover, an array of 25 microphones, equally distributed from 0 to 120 deg along an arc of radius 18.5 m centered on the fan axis at the nozzle inlet, was used for far-field sound measurements upstream of the inlet. Hot-wire (HW) measurements were performed upstream of the fan (HW0 position) and in the interstage at different axial locations (HW1, HW2, and HW3 positions for the long-gap configuration, and only the HW1 for the short-gap configuration). Both configurations were tested at different operating conditions (approach, sideline, and cut-back conditions) on two different working lines (sea level static and low noise) that differ by the blade loading of the fan. The present paper focuses exclusively on the sea level static working line, at approach condition, for the short-gap configuration. The hot geometry of the fan blades, which accounts for the deformation of the fan blades induced by the rotational speed, is used in the present study. The flow conditions at this operating point as well as some details about the stage geometry are given in Table 1.

III. Simulations Setup

A. Computational Domain

To limit the computational costs of the simulation, computational domains for turbomachines are commonly reduced using periodic boundary conditions. In the particular case of the TurboAVBP solver used in the present study, the rotor–stator interface requires to have the same angular sector for the rotor and stator domains. For the ACAT1 geometry, the domain can thus be reduced to a quarter of the geometry, consisting of 5 fan blades and 11 vanes. Nevertheless, a domain covering 5–11 channels is still too large for a full three-dimensional (3D) fan-OGV stage resolution. To further reduce the

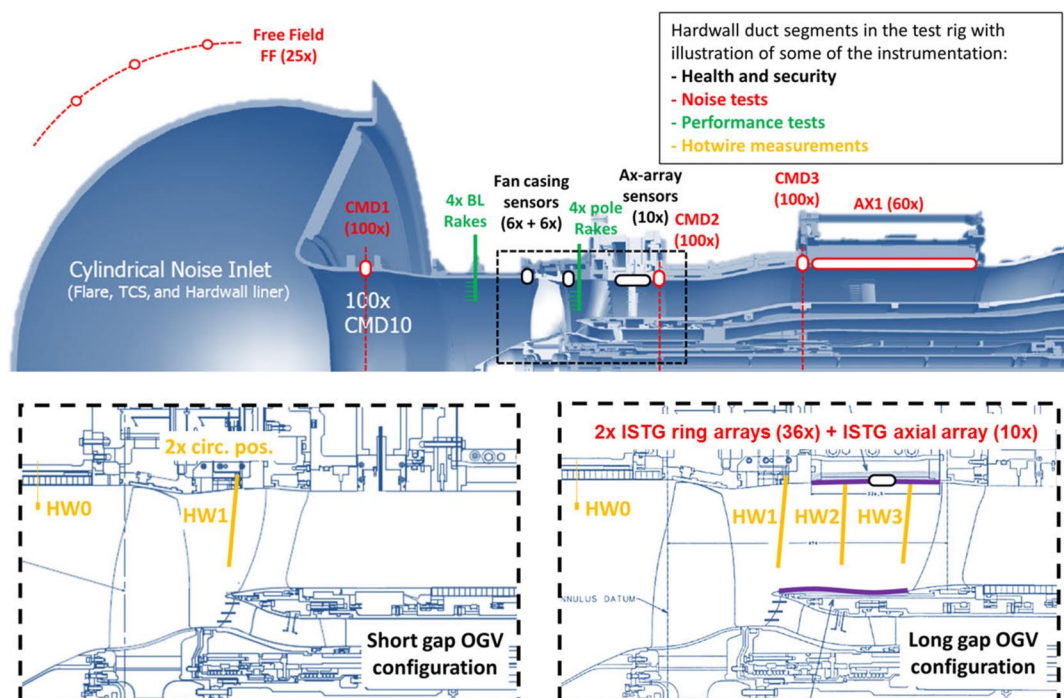


Fig. 1 View of the UFFA fan rig of AneCom AeroTest.

Table 1 Approach condition

<i>Geometrical parameters</i>	
Tip radius (m)	0.435
Hub radius at the rotor leading edge (m)	0.138
Rotor midspan chord, $c_{R,\text{midspan}}$ (m)	0.136
Stator midspan chord, $c_{S,\text{midspan}}$ (m)	0.066
Rotor tip gap (mm)	0.78
Rotor–stator spacing	$\approx 1.3c_{R,\text{midspan}}$
<i>Operating point</i>	
Rotational speed (rpm)	3828.2
Tip relative Mach number	0.57
Total mass-flow rate (kg/s)	55.156
Bypass ratio	7.6
Ambient pressure (hPa)	995.6
Ambient temperature (K)	292.8

computational domain, a modification of the vane count, reducing it from 44 to 40 (9% reduction) has been performed. This resulted in a 1 rotor blade-2 stator vane configuration ($2\pi/20$ periodicity), which leads to a significant reduction of the computational costs. To maintain the stage performance while reducing the vane count, the stator vanes are rescaled to keep the same solidity as the original OGV according to Rai and Madavan [29]. This modification, performed by ONERA [30], consists of an axial rescaling (9% chord increase) and an azimuthal rescaling by the same factor. The leading-edge position remains the same in order to maintain the fan-OGV distance of the original configuration. The camber line and the thickness-to-chord ratio are also conserved. Determinant parameters for broadband noise predictions, such as sweep, lean, and stagger angles, are also maintained. Because the vane count is modified, such a geometric transformation will have a significant impact on the tonal component of the noise but the blade passing frequencies (BPFs) will remain unchanged. However, it only has a limited impact on the broadband noise as shown by Leonard et al. [4], who performed a similar geometric transformation on the source diagnostic test (SDT) configuration. This can also be verified by the analytical models described hereafter.

The meridional view and a 3D view of the computational domain are depicted in Figs. 2 and 3.

The short interstage configuration is chosen. It consists of 20 fan blades and 40 rescaled vanes. The fan tip gap is 0.78 mm. The inlet guide vanes (IGVs) of the primary flow have been removed from the computational domain, because the broadband noise resulting from its interaction with the fan is considered as relatively negligible.

The computational domain extends from four fan axial chords upstream of the rotor at midspan, to six vane axial chords downstream of the stator also at midspan. Two main reasons have led to the choice of these dimensions:

- 1) They allow the boundary layers to develop on both the spinner and the casing upstream of the rotor.
- 2) The core and bypass exhaust boundary conditions are easier to control especially regarding the reflection of sound waves.

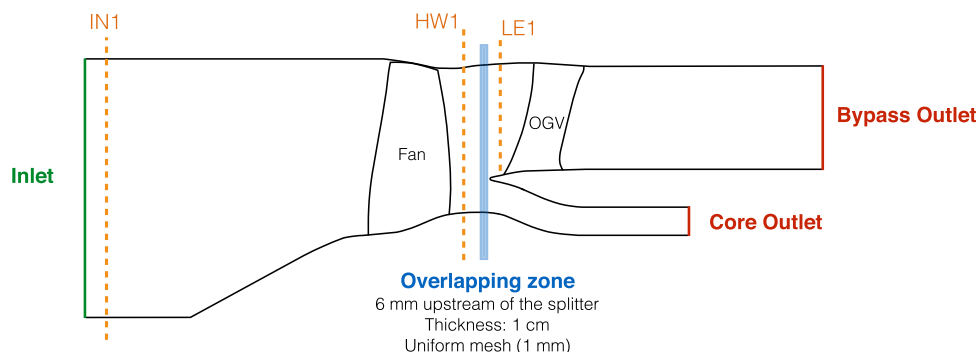


Fig. 2 Computational domain. IN1, HW1, and LE1 correspond to the location of the axial cuts performed in the LES simulations. HW1 is also the location where the hot-wire measurements have been performed.

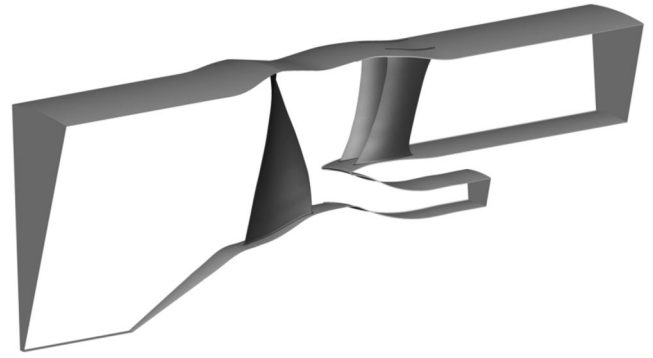


Fig. 3 Three-dimensional view of the computational domain.

B. Unstructured Mesh

The mesh is a hybrid unstructured grid composed of eight prism cells on walls, to accurately resolve the boundary layers, and of tetrahedral cells in the rest of the domain. The choice of the number of prism layers is consistent with the current state-of-the-art of wall-modeled LES for fan-OGV simulations (see [19,31–33]). Volume and surface refinements have also been introduced in order to ensure the quality of the mesh. Surface refinements have been mainly used to accurately discretize the blades and the vanes, especially the leading edges, the trailing edges, and the fillets. This has resulted in a rotor mesh with more than 150 cells in the axial direction and 200 cells in the radial direction. For the stator domain, there are at least 100 cells in the axial direction and more than 150 in the radial direction. In the case of wall-modeled LES, the dimensionless wall distance to a surface in the normal direction (designated equivalently by y^+ or n^+) and in the tangential directions (s^+ for the streamwise direction and r^+ for the third local direction) have to meet certain requirements that are recalled in Table 2 along with the wall-resolved LES requirements.

The n^+ values in the entire computational domain are shown in Fig. 4. Figures 5 and 6 show a closer look at the n^+ , s^+ , and r^+ values on the blade and vane skins, confirming that the mesh is consistent with the wall requirements for wall-modeled LES.

Four main volume refinement blocks have been used on both the fan and the OGV:

- 1) Wake refinements to correctly transport the wakes down to the rotor–stator interface. This has guaranteed at least 15 points in the wake that ensures an accurate description of the physics.
- 2) Leading-edge and trailing-edge refinements to ensure a smooth transition from the fine mesh near the walls to the coarser mesh in the interblade channel.
- 3) Tip gap refinements: About 20 cells have been used to discretize this region.
- 4) Interblade region refinements to guarantee a correct azimuthal description of the flow with at least 120 cells per sector.

The final mesh is displayed in Figs. 7–9. The apparent zigzag roughness is an artifact of the plotting software and of the chosen cut. These parameters eventually lead to a mesh composed of 55 million

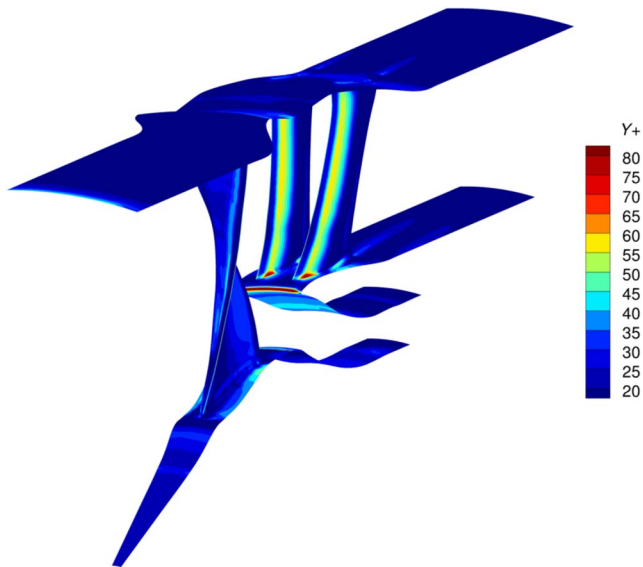
Fig. 4 Values of n^+ .

Table 2 Wall mesh requirements for LES [34,35]

Dimensionless distances	Wall-resolved LES	Wall-modeled LES
s^+	50–150	100–600
r^+	10–40	100–300
n^+	1	30–150
No. of points in $0 < n^+ < 10$	3–5	—

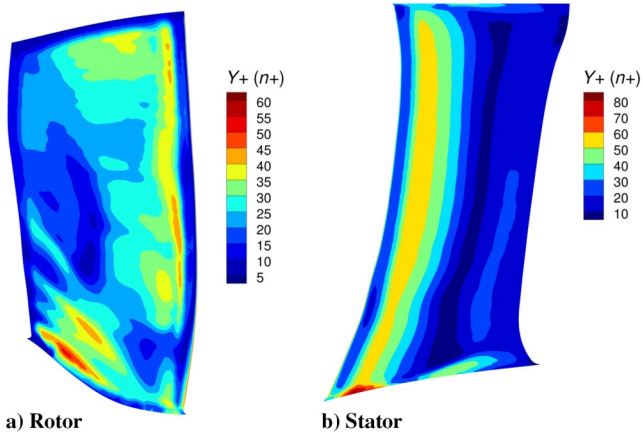
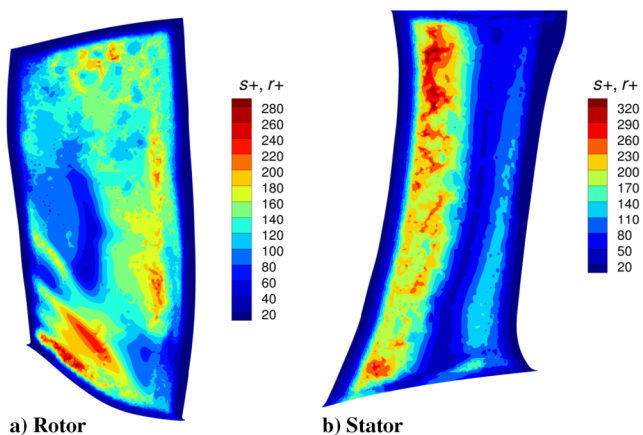
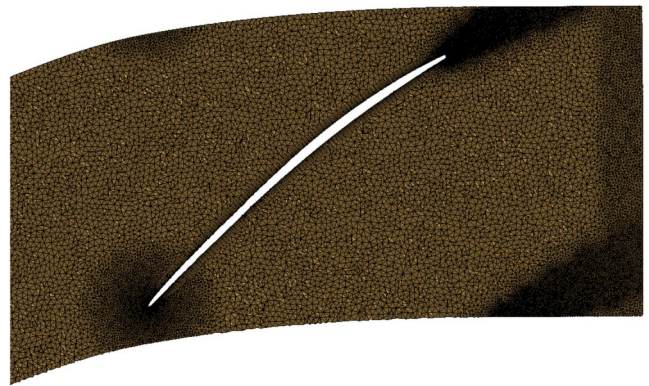
Fig. 5 Values of n^+ on the rotor and stator suction sides.Fig. 6 Values of s^+ and r^+ , rotor and stator suction sides.

Fig. 7 Midspan radial cut of the rotor domain mesh.

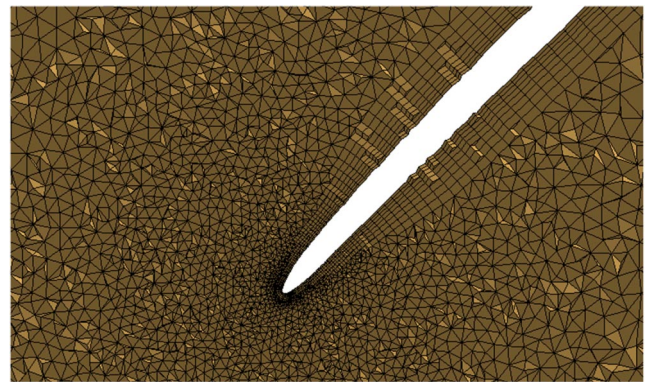


Fig. 8 Rotor blade leading-edge mesh.

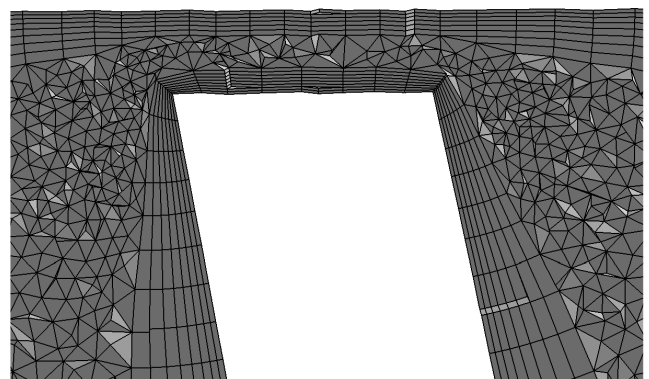


Fig. 9 Rotor blade tip gap mesh.

cells in the rotor domain and of 40 million cells in the stator domain. To avoid the unnecessary oversizing of the mesh observed on the RANS mesh [24], an optimized meshing approach based on the RANS velocity field of the wake has been used to create refinement blocks fitted to the wake, consequently reducing the CPU cost of the simulation. For this medium-sized mesh, a maximum cell size of 2 mm has been imposed so that acoustic waves up to 10 kHz (8 blade passing frequencies [BPFs]) are propagated with at least 25 points per wavelength. In terms of mesh quality the equivolume skewness has been maintained below 1, which guarantees that there are no degenerate cells. Similarly, the equiangle skewness is kept below 0.95, which is the limit to sliver cells.

C. Large-Eddy Simulation

1. Solver- and Simulation-Specific Features

The turbomachinery capacity of the AVBP code developed by Cerfacs [36] has been used to carry out the compressible LES on the

ACAT1 configuration. The method used consists of the coupling of two LES domains: the first one dedicated to the rotor and the second one to the stator. The two computational domains are coupled using an overset grid method [37], implemented using the coupling library CWIPI, through which conservative variables are exchanged between the two instances.

The filtered compressible Navier–Stokes equations describing the mass, momentum, and energy equations for a perfect gas are solved. Equations are solved using a finite-volume Lax–Wendroff time explicit scheme with second-order accuracy in time and space [38]. The wall-adapting local eddy viscosity (WALE) subgrid-scale closure, developed by Nicoud and Ducros [39], is used to model the unresolved turbulent contributions. The inlet and outlets are treated using nonreflecting characteristics boundary conditions (Navier–Stokes characteristic boundary conditions (NSCBC)) [40]. At the inlet, the experimentally measured total temperature and pressure are imposed and the flow is purely axial with no turbulence injection [41]. At the outlet, the flow reaches a radial equilibrium that matches the mean static pressure extracted from a surface average of the static pressure at the outlet of the RANS simulation. Periodic boundaries are imposed on both lateral sides of the domain.

On all the solid walls, the boundary layer is modeled using a wall law inducing a no-slip condition at the walls (see the work of Nicoud et al. [42] for more details on the law itself). A linear law is imposed if the normalized wall distance satisfies the condition $y^+ < 11$, and a logarithmic law otherwise [43]. In the present case, the mean y^+ is close to 35, which is a satisfactory value for wall-modeled LES [34].

The simulation has been initialized using the RANS solution of Lewis et al. [24] in order to reduce the transient period of the simulation. The time step for the simulation has been set to 3.7×10^{-5} ms to obtain around 22,000 iterations per blade passage. The present numerical methodology has been validated on compressors [44], turbines [45], and turbfans [4,19,31,33].

2. Convergence Check

The convergence state of the simulation has been checked by monitoring common integrated quantities (mass-flow rate at the inlet and outlets, pressure ratios in the bypass and core flows) as well as local quantities such as the pressure or the velocity using local control points (hereafter referred to as “probes”), the locations of which are indicated in Fig. 10. The stabilization of integrated quantities ensures the convergence of the mean flow. As was performed by Leonard et al. on the SDT configuration [4], the convergence of flow statistics was checked by analyzing the pressure signals retrieved from the probes with the method developed by Mockett et al. [46]. This method can be used to estimate the statistical error of a finite time signal and is particularly suited to identify the end of the transient regime of an LES. It has been applied to all the probes to estimate the best time to start recording the statistics of the actual simulation. The transient regime lasted around 5.5 full rotor revolutions, and the statistics were recorded for about 4 rotations.

Over these four rotations, the wall pressure fluctuations on the rotor blades and the stator vanes have been recorded as well as the pressure and the velocity components at the three axial positions shown in Fig. 2 (IN1, HW1, and LE1) in order to be postprocessed. These flow extractions have been performed every 250 time steps, which corresponds to a sampling rate of about 110 kHz.

IV. Aerodynamic Analysis

The results obtained from the LES are presented in the following sections. Results are compared with both the experimental performance parameters and the HW measurements.

A. Global Performance

Tables 3 and 4 summarize the performance parameters at approach condition obtained from the LES. These values were obtained from a mass-flow rate weighted average over an axial field cut at the splitter location, upstream of the stator. The agreement of the LES results with the experimental data is excellent, showing negligible discrepancies for both the mass-flow rates and the pressure ratios.

B. Mean Flow

1. Flow Topology

A first overview of the mean flow topology is depicted in Figs. 11a and 11b, which show streamlines of the mean flow colored by the mean vorticity magnitude on the rotor and stator suction sides, respectively. The rotor streamlines are shown in the relative frame of reference. A significant radial flow can be observed in the rotor domain, especially at the leading edge where a strong radial vortical structure, covering almost 80% of the fan span, appears. The fact that the leading-edge streamlines move alternatively toward the upstream and downstream directions suggests that this structure corresponds to a strong recirculation region. This vortical structure appears to be partly formed of streamlines originating from the lower part of the fan leading-edge and traveling up to the rotor tip, where they eventually feed the tip gap flow. Such a radial structure was also observed in Kissner et al.’s RANS study on the ACAT1 fan stage at approach condition (see Fig. 5 in [11]), and by Pérez Arroyo et al. [47] on the SDT configuration also at approach condition, suggesting that it is a characteristic flow feature at low fan speeds. In the stator domain, the streamlines are aligned with the stage axis down to 60% chord, where a radial vortical structure, similar to that observed in the rotor domain, appears. Its structure suggests that it corresponds to a region of intense recirculation partly formed of streamlines originating from the hub and shroud boundary layers. Apart from these areas that

Table 3 Mass-flow rates obtained at approach condition

	Mass-flow rate (kg/s)		
	Bypass	Core	Total
Experiment	48.745	6.411	55.156
RANS	48.745	6.411	55.156
LES	48.787 (+0.09%)	6.395 (−0.25%)	55.186 (+0.05%)

Table 4 Fan pressure ratios obtained at approach condition

	Fan pressure ratio		
	Bypass	Core	Total
Experiment	1.110	1.100	1.109
RANS	1.106 (−0.36%)	1.098 (−0.2%)	1.105 (−0.36%)
LES	1.106 (−0.36%)	1.095 (−0.45%)	1.105 (−0.36%)

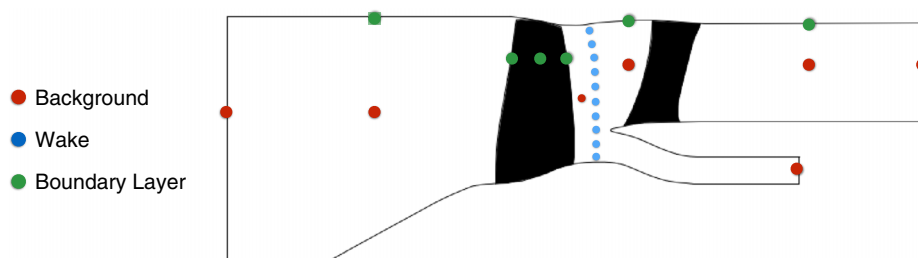


Fig. 10 Probe locations.

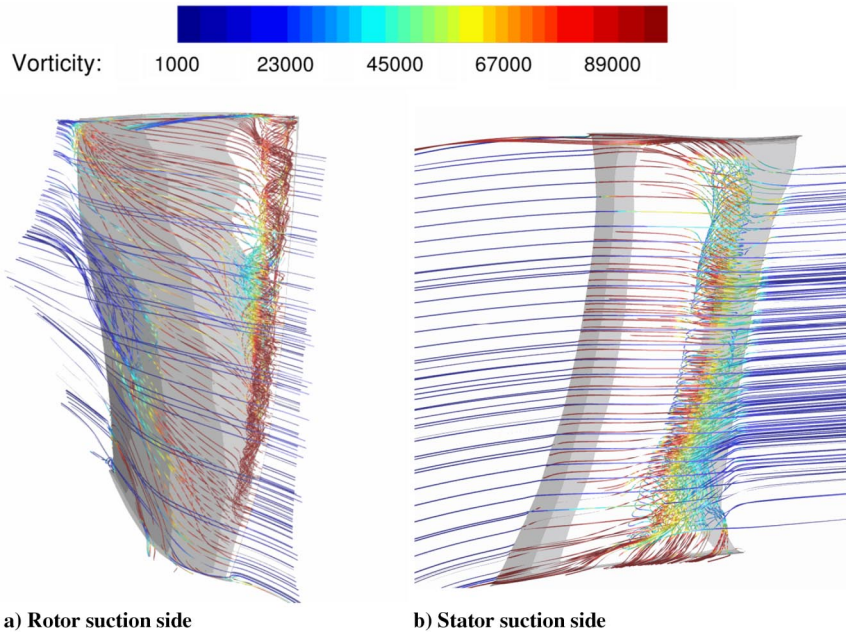


Fig. 11 Streamlines of the mean flow colored by the vorticity magnitude.

exhibit a flow separation, the flow remains attached on most of the rotor and stator surfaces. The identified recirculation regions significantly contribute to the creation of turbulent structures in the vicinity

of the blade and vane surfaces as shown by the Q -criterion isosurfaces displayed in Figs. 12 and 13. The leading-edge flow separation on the rotor results in a strong boundary-layer transition and generates a

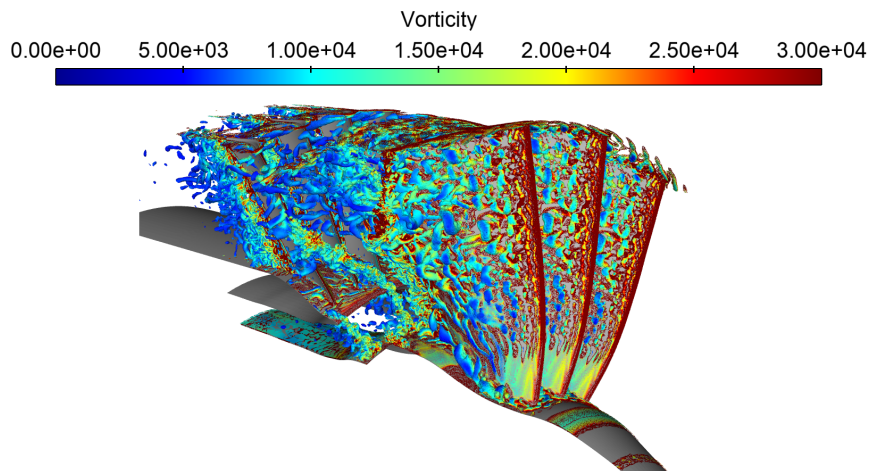


Fig. 12 Q -criterion isosurface ($7 \times 10^6 \text{ s}^{-2}$) colored by the vorticity magnitude. Rotor view.

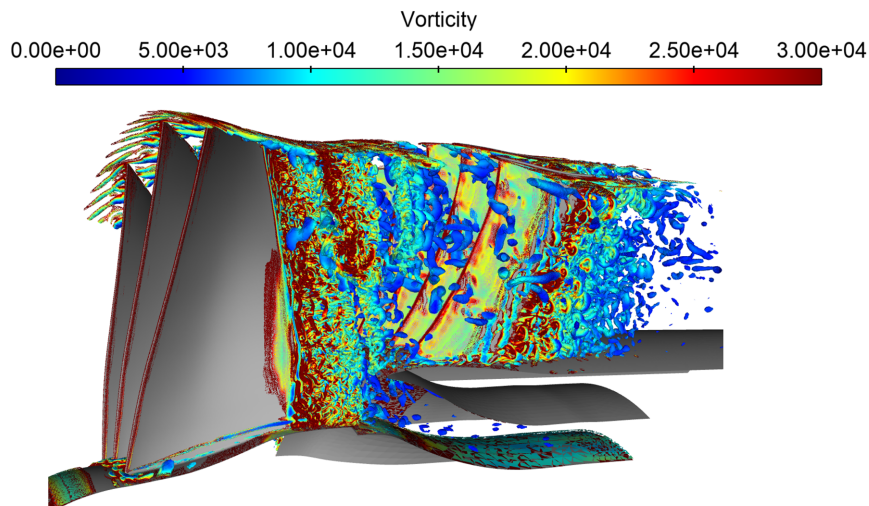


Fig. 13 Q -criterion isosurface ($7 \times 10^6 \text{ s}^{-2}$) colored by the vorticity magnitude. Stator view.

wide range of turbulent structures that graze along the rotor suction side down to the trailing edge, where it interacts with the wake. Such a boundary-layer transition can also be clearly observed on the stator suction side, at the same location as the recirculation region.

2. Friction Line Analysis

As the flow speed is reduced at approach condition with respect to cruise condition, higher angles of attack can be observed at the fan leading edge, which generally results in local flow separations as highlighted in the previous section. To better identify these detached zones, the mean friction coefficient C_f has been computed on the suction side of the blades and vanes and is displayed in Figs. 14a and 14b, respectively, along with the streaklines. C_f is defined as follows:

$$C_f = \frac{\tau_w}{(1/2)\rho_\infty V_\infty^2} \quad (1)$$

where ρ_∞ and V_∞ are the density and the velocity of the fluid at the inlet, respectively. τ_w is the wall shear stress defined as

$$\tau_w = \mu \left(\frac{\partial V_s}{\partial n} \right)_{\text{wall}} \quad (2)$$

where μ is the dynamic viscosity of the fluid, V_s is the flow velocity tangent to the wall, and $(\partial V_s / \partial n)_{\text{wall}}$ is the wall value of the derivative of V_s in the wall-normal direction.

As expected, a leading-edge flow separation appears from 20% of the fan span up to the tip of the rotor. The flow reattaches before reaching a quarter of the blade chord and remains attached down to the trailing edge on most of the fan span. Such a flow separation was also observed on the ACAT1 fan stage at approach condition using other simulation approaches such as Zonal Detached Eddy Simulation (ZDES) (see [14,30]), Zonal Large Eddy Simulation (ZLES) (see Fig. 11 in Tucker and Wang's review paper [48]), and RANS (see [11]). Between 30 and 60% of the rotor span, however, a large flow detachment occurs from 60% of the axial chord down to the trailing edge. Regarding the vane, the flow remains attached until it reaches half of the vane chord where a flow detachment covering almost all the vane span occurs. This flow separation was not predicted by the RANS simulation [24]. Between 20 and 95% of the vane span, the flow reattaches before reaching the trailing edge, whereas under 20% it remains detached.

3. Fan Wake Analysis

Broadband interaction noise directly depends on the turbulent state of the flow impacting the stator row. As a consequence, typical

turbulence variables such as the turbulent kinetic energy (TKE) within and outside of the wakes, and the flow characteristic dimensions (wake width, integral length scale) are usually prescribed as input parameters for analytical models. They notably have a substantial effect on the subsequent noise predictions [4,49]. An accurate simulation of these flow characteristics is thus compulsory to ensure the reliability of the noise predictions, whether numerical or analytical. Because of a HW calibration issue during the AneCom tests, a post-test recalibration was performed on the raw data by the team in charge of the measurements to correct a detected offset, giving rise to the more reliable data that are used in the present study. Figure 15 shows the average values of the three velocity components and of the TKE measured by the HW at the HW1 position retrieved from the recalibrated data set. The axial velocity (Fig. 15a) and TKE (Fig. 15d) contours reveal significant wake-to-wake variations: some blades are shedding particularly thick wakes with intense TKE levels (wake at 4 o'clock), whereas others produce very thin wakes with low TKE levels (wake at 10 o'clock). Slight blade-to-blade geometrical differences in the experiment, in conjunction with the choice of an operating point close to surge, may have affected the leading-edge rotor flow separation in terms of magnitude and chordwise extent, resulting in downstream wake disparities. This non-axisymmetry prevents from precisely appreciating the wake similarities and disparities with the simulations. To have a quantitative analysis, the mean and root mean square (RMS) azimuthal profiles of each velocity component have been plotted for different radial positions, along with the corresponding experimental revolution range. The latter is basically the area delimiting the range of variations observed in the experimental data at each radius, and over the full annulus. Thereby, the blade-to-blade variations are taken into account without isolating each wake.

At 25% rotor span (Fig. 16), the experimental revolution range is remarkably thinner than at other radial positions, indicating smaller blade-to-blade variations and a weaker flow detachment. Regarding the axial velocity, the LES underestimates the velocity deficit, which may result from upstream flow detachment intensity disparities in the LES with respect to the experiment. The LES also slightly overestimates the background values. The simulation tends to predict a thinner wake than in the experiment. Both azimuthal and radial velocities are overestimated by the LES, which could be partly explained by the absence of the IGV in the LES setup. The overall shape of the experimental profile is well recovered, which ensures that the correct behavior of the flow is captured. However, an unexpected hump can be observed at 50% of the passage. The wake RMS values are overestimated at this radius by a factor 2–3. As a whole, the RMS profiles are sharper than the experimental ones and the background values are well captured.

At 50% rotor span (Fig. 17), the axial velocity deficit and the wake width are this time well captured by the LES. An overestimation of the background axial velocity is, however, observed. This overestimation of the background velocity is actually noticed over almost the whole blade span, which indicates a mismatch between the HW and the performance measurements. The azimuthal velocity profile is in good agreement with the experimental data. The radial velocity is still overpredicted at this radial position, but is in better agreement with the experimental measurements than at 25% rotor span. These remaining discrepancies for the radial velocity component might be partially explained by the lack of accuracy of the experimental estimate using HWs, because comparable discrepancies have been observed on RANS studies on the ACAT1 fan stage (see Kissner et al. [11] for a comprehensive comparison of all available RANS simulations) and on other configurations [50]. The radial velocity is indeed very small compared with the two other components; therefore slight differences in the main components account for relatively large variations of the radial velocity. The wake RMS values are again overestimated for each component. Nevertheless, the LES results display profile shapes that faithfully reproduce those observed in the experiment.

The significant blade-to-blade variations observed at 75% rotor span (Fig. 18) result in a wide experimental revolution range. At this radial position, the experimental axial velocity deficit and the wake width are well recovered by the simulation. The background velocity is, however, still overestimated. The circumferential velocity profile

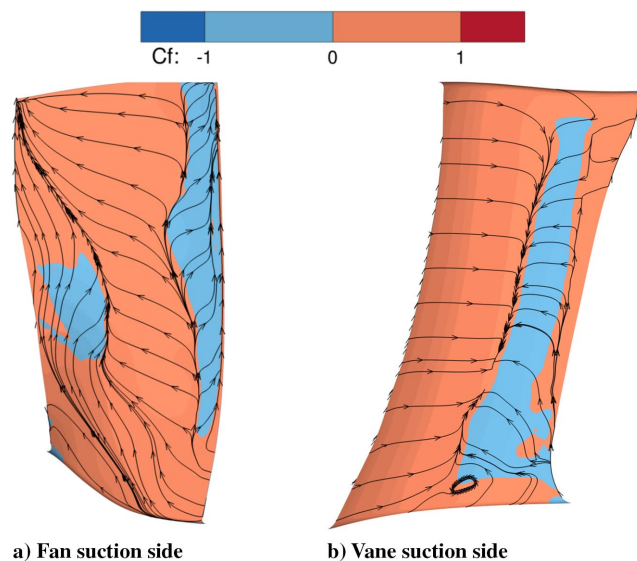


Fig. 14 Mean friction coefficient and streaklines.

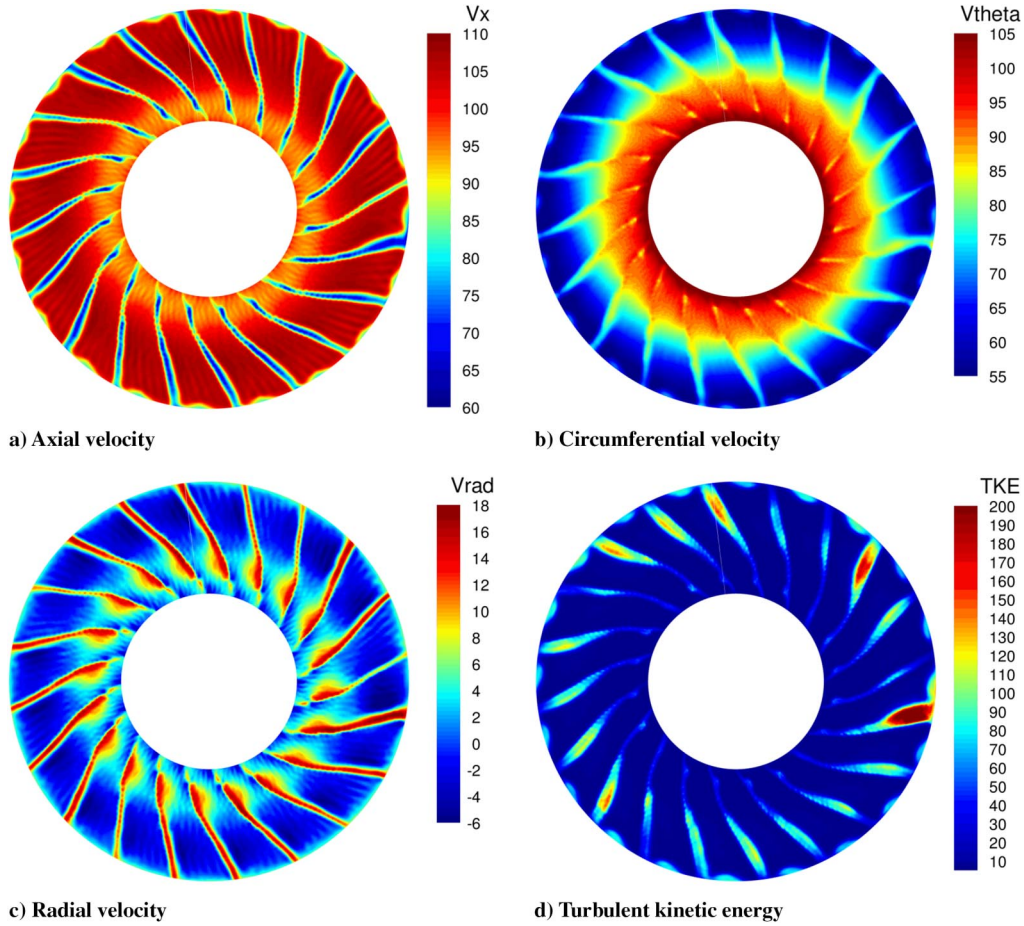


Fig. 15 Hot-wire measurements at position HW1.

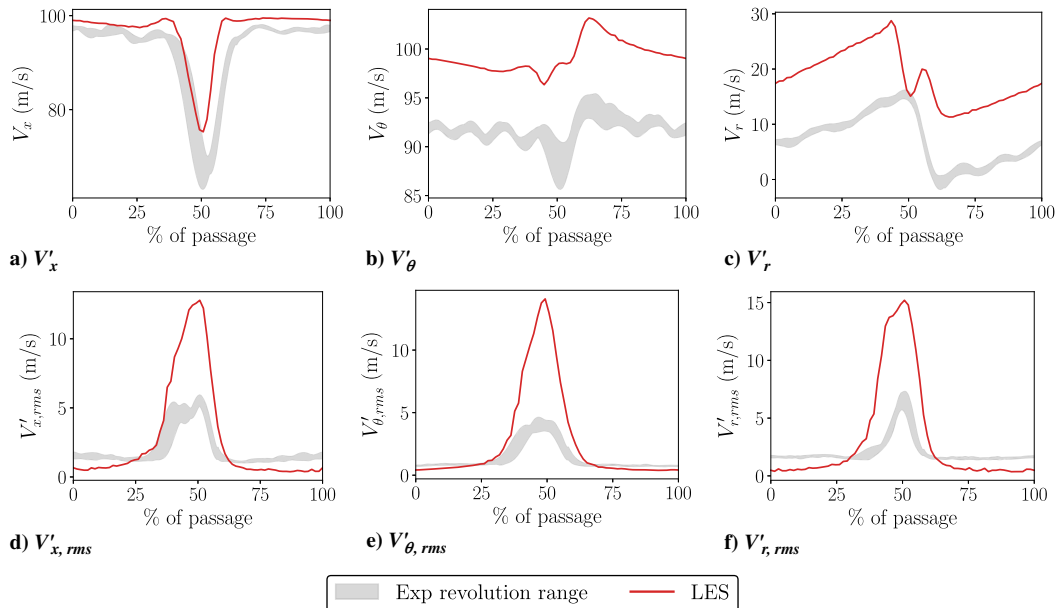


Fig. 16 Velocity component azimuthal profiles at 25% rotor span.

is in good agreement with the experimental data, but slightly overestimated in the background flow. The radial velocity is still overpredicted, but a much better agreement with the experimental data is observed with respect to other radial positions. Concerning the RMS profiles, similarly to what has been observed at 50% rotor span, the LES predicts profiles with shapes faithfully reproducing the experimental ones. In terms of magnitude, the LES provides higher values

for the radial and azimuthal components but is much closer to the experiment than at 50% span. For the axial component, however, the computed values are of the same order as the experimental ones.

Finally, the radial position located at 95% rotor span (Fig. 19) shows that the LES is in good agreement with the measurements in terms of magnitude and shape for the axial and azimuthal velocity components, whereas the radial component is still overestimated.

Important blade-to-blade variations are observed for the experimental RMS values, as indicated by the wide experimental revolution range. This makes the reading of the results more difficult but still shows that the shape of the profiles is well captured by the LES for all velocity components. In terms of magnitude, the LES tends to overestimate the RMS levels for all components, but much less than at 25 and 50% rotor span.

To get an additional insight into the radial distribution of the mean flow velocity components across the duct channel, the radial mean velocity and RMS profiles of each velocity component are provided in Fig. 20. Both axial and circumferential velocity components are in good agreement with the measurements. As already highlighted with the azimuthal profiles (Figs. 16c, 17c, 18c, and 19c), the radial component of the velocity is overestimated especially between 10 and 70% of the duct channel height. The shape of the RMS profiles is very similar to that of the measurements. The magnitude is, however, overestimated close to the hub and between 40 and 70% channel height. Lewis et al.'s RANS results [24] are also plotted in Fig. 20. The RANS and LES mean velocity component profiles are very

similar. However, some disparities appear when comparing the RMS profiles, especially at midspan where the LES predicts larger values with respect to the RANS simulation.

The overall agreement of the LES with the experiment regarding the mean velocity components is quite satisfactory given the lack of accuracy of the HW technique and the calibration issues reported during the experiment. Nevertheless, the RMS levels are significantly overestimated over most of the blade span, even though the shape of the profiles seems to be well captured. Studies on the same case by François et al. [30] and by Polacsek et al. [14] have shown similar discrepancies with the experimental data using a ZDES approach with a 380-million-cell mesh, unveiling a potential lack of accuracy of the HW measurements regarding the velocity fluctuations. This was confirmed by Polacsek et al.'s [14] deeper analysis of the velocity spectra, which revealed that the thickness of the HWs induced a cutoff frequency that resulted in an underestimation of the real velocity fluctuations by an estimated factor of 1.5 at 50% rotor span. Considering this correcting factor, the agreement of the present results with the experiment is much better (see Fig. 21), even though

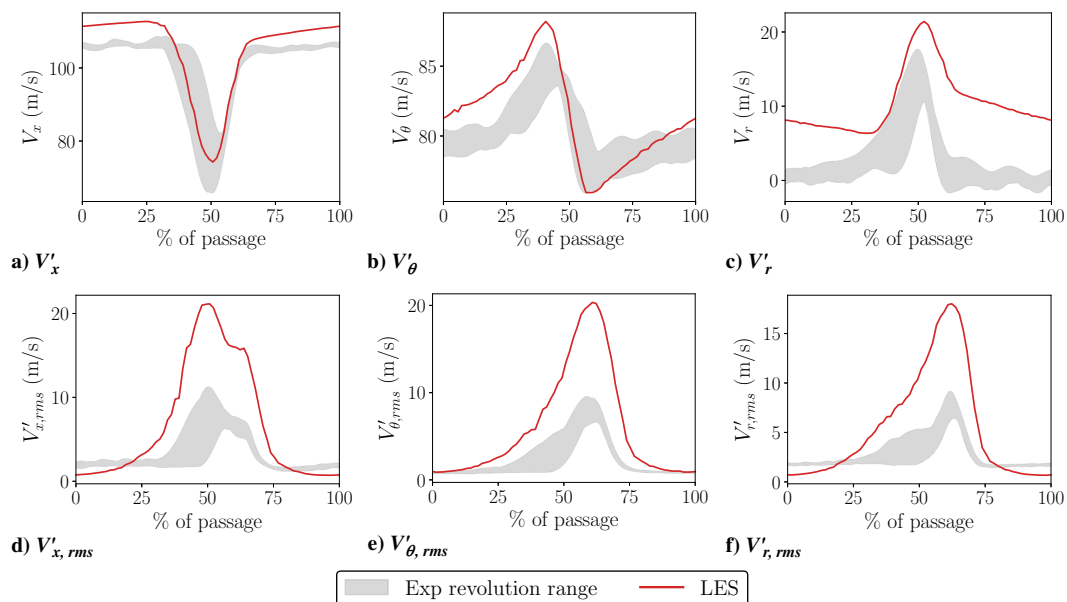


Fig. 17 Velocity component azimuthal profiles at 50% rotor span.

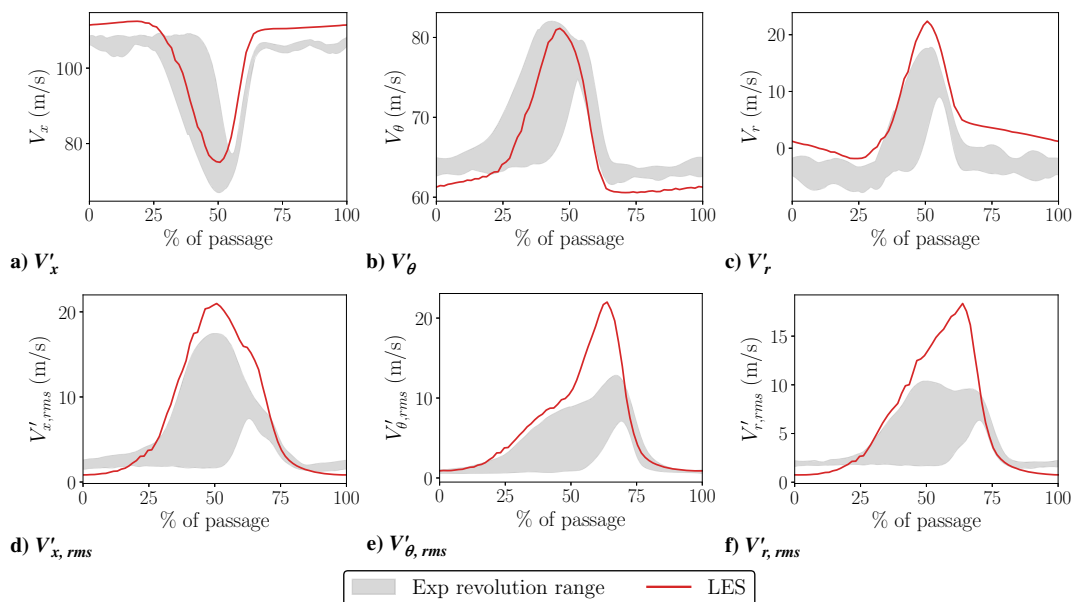


Fig. 18 Velocity component azimuthal profiles at 75% rotor span.

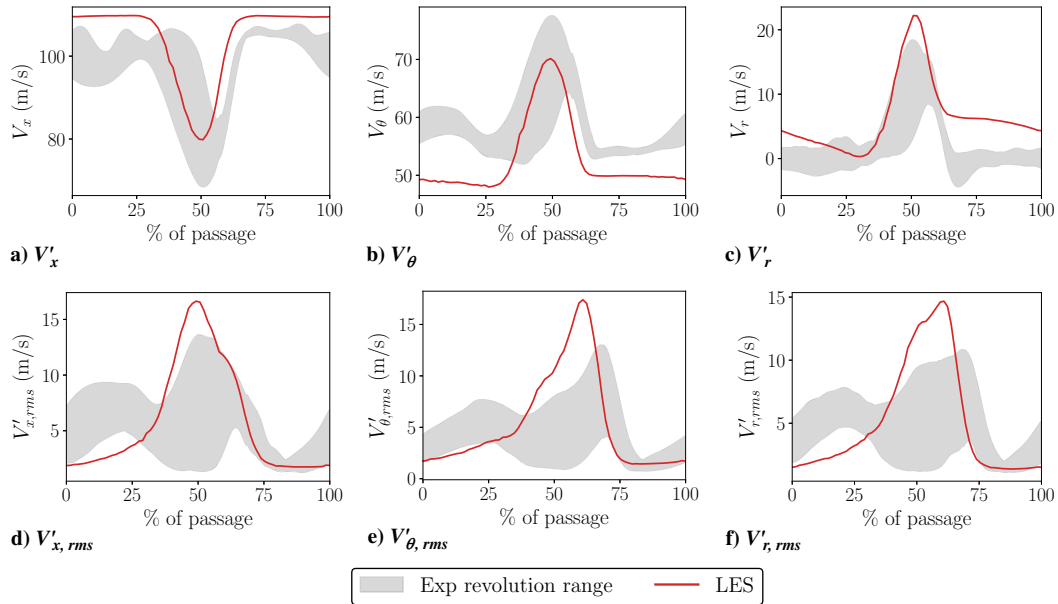


Fig. 19 Velocity component azimuthal profiles at 95% rotor span.

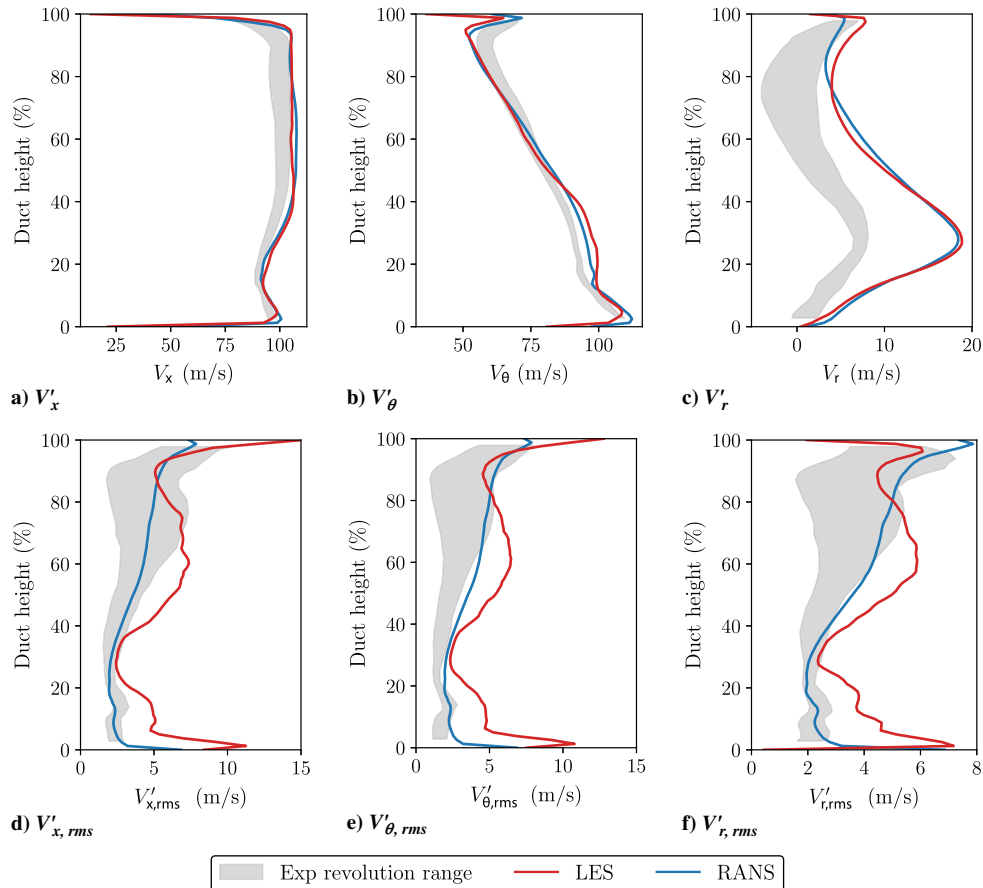


Fig. 20 Velocity component radial profiles at HW1 position.

a slight overestimation remains. Figure 22 shows the comparison of the radial RMS profiles with the corrected measurements assuming that the estimated 1.5 factor is valid over the entire span. The agreement of the radial profiles with the experimental data is much better, with only a slight overestimation observed at midspan and close to the hub. Lewis et al.'s RANS results remain within the corrected experimental revolution range, with a slight underestimation below 30% duct height.

V. Broadband Noise Predictions Using Analytical Models

This section presents the LES-informed analytical predictions that have been performed. The objective is to assess the impact on the noise predictions of the use of the more accurate LES input parameters, with respect to the RANS-informed predictions performed previously [24].

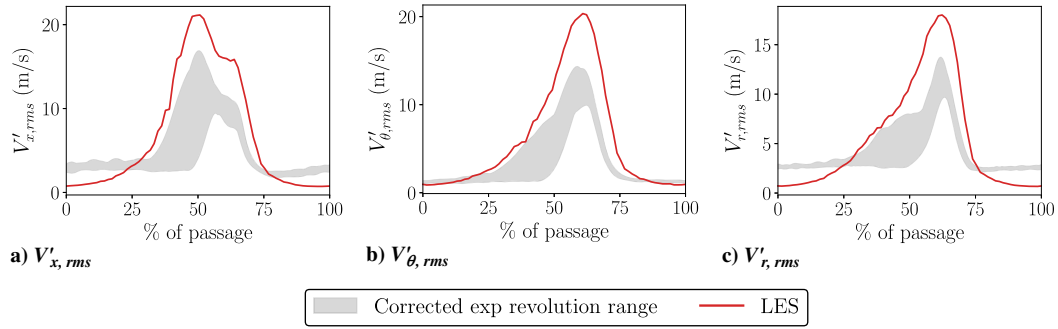


Fig. 21 RMS azimuthal profiles at 50% rotor span with corrected experimental data (1.5 factor).

A. Extraction of Input Data for Acoustic Models

Analytical models require several input parameters in order to reconstruct the stator incident flow and compute the resulting loading fluctuations:

- 1) The axial velocity
- 2) The absolute velocity
- 3) The turbulence intensity (TI) in the wake and the background flow
- 4) The turbulence integral length scale (TLS) in the wake and the background flow
- 5) The wake half width

These flow parameters have been retrieved from the LES thanks to an axial cut located at the LE1 position (see Fig. 2). This cut has been performed as close as possible to the stator leading edge in order to get a representative description of the flow that is actually interacting with the vane cascade. A well-adapted and practical way to extract these parameters is to assume a Gaussian shape for the wake, based either on the absolute velocity deficit or on the TKE. Performing a Gaussian fit on the extracted wakes then enables the separation of the background flow from the wake variables by applying a 20% threshold (see Fig. 23).

Multiple processes for estimating the streamwise turbulence lengthscale based on numerical simulations are available. For RANS simulations, the first one, proposed by Pope [51], makes direct use of the turbulent variables k and ω through the following relationship:

$$\Lambda_p = C_{Re} \frac{\sqrt{k}}{C_\mu \omega} \quad (3)$$

with $C_{Re} = 0.43$ and $C_\mu = 0.09$. Another estimate can be obtained using the wake width L_w with the empirical relationship of Jurdic et al. [52]:

$$\Lambda_j = 0.21 L_w \quad (4)$$

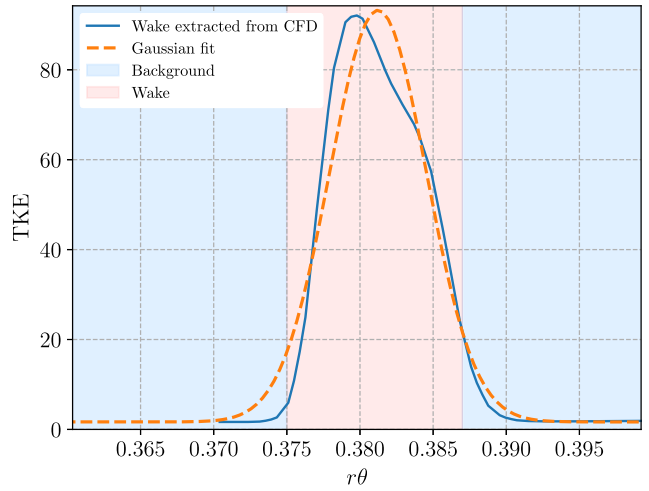


Fig. 23 Wake extraction using a Gaussian fit.

where L_w corresponds to the full width at half maximum of the Gaussian function used for the fitting process, and it is computed using the standard deviation σ of the Gaussian function through the following relationship: $L_w = 2\sqrt{2\ln(2)}\sigma$. The wake and background TLS are the same when using this estimate. It can obviously be used also when retrieving data from LES. Another integral length scale estimate can be obtained using the unsteady data extracted from the temporal recording made on an axial cut through the computation of the temporal autocorrelation function:

$$R_{uu}(\mathbf{x}, \tau) = \frac{\overline{u'(\mathbf{x}, t)u'(\mathbf{x}, t + \tau)}}{u_{rms}^2(\mathbf{x})} \quad (5)$$

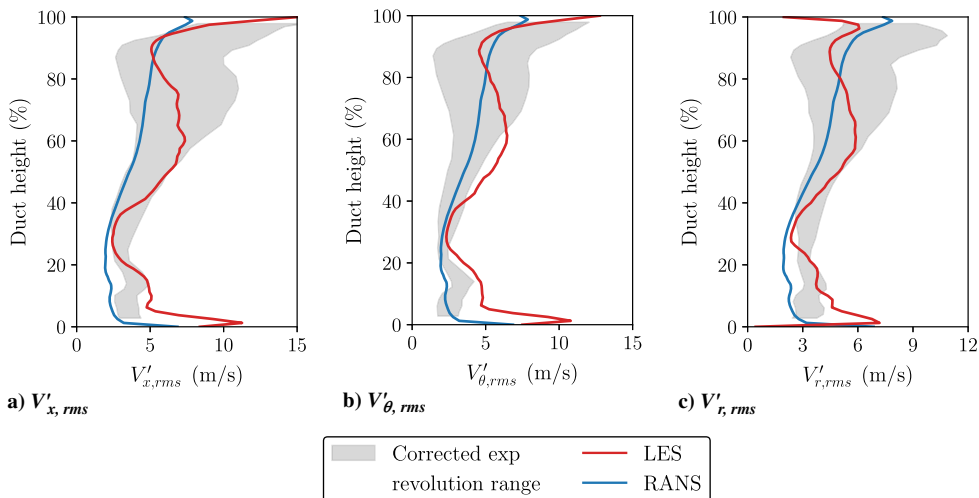


Fig. 22 Velocity component radial profiles at HW1 position with corrected experimental data (1.5 factor).

where $u'(x, t)$ is the axial velocity fluctuation at position x and time t , and $u'_{\text{rms}}(x)$ the root-mean-square velocity fluctuations at position x . The autocorrelation can then be used to compute the temporal integral scale [51]:

$$\Lambda_t = \int_{\tau=0}^{\infty} R_{uu}(x, \tau) d\tau \quad (6)$$

Under Taylor's frozen turbulence assumption [51,52], an axial integral length scale can finally be computed as follows:

$$\Lambda_c = \bar{U} \Lambda_t \quad (7)$$

where \bar{U} is the mean axial velocity transporting the turbulence. Other TLS estimates relying on spatial correlations also exist but have not been investigated in the present study. Some of them were thoroughly studied by Grace et al. [8], who assessed their impact on analytical broadband RSI noise predictions.

To compute the TLS from the LES using Λ_j , a phase-locked average has been performed over about four rotations on the axial cut upstream of the OGV leading edge at the LE1 position (see Fig. 24). The Λ_c estimate was also computed on the same axial cut and over the same simulation time. The latter estimate was performed using the same approach as Odier et al. [31] in the rotor-locked reference frame so that the wake could be separated from the background flow using the previously described Gaussian fitting process.

Figures 25 and 26 show the radial distribution of the input parameters resulting from the previously explained extraction processes. The LES values are plotted along with the RANS extractions that were performed by Lewis et al. [24] for the same case. It should be noted that the RANS flow was first extrapolated from the rotor domain down to the stator leading edge, using Jaron et al.'s method [53], in order to get a realistic flow at the stator leading edge in spite of using a mixing plane approach. Nevertheless, because the distance between the leading edge and the axial cut of the LES is relatively small, the flow disparities between these two positions are expected to be relatively small as well, which ensures a reliable comparison between the two extractions.

The absolute and axial velocities (Figs. 25a and 25b, respectively) extracted from the LES and the RANS are relatively similar, with values that are slightly higher at the stator midspan for the RANS. The TI, however, shows significant disparities. On the one hand, the background TI (Fig. 25c) of the LES is slightly lower than for the RANS. This may be because no turbulence has been prescribed at the inlet of the LES, whereas an inlet TI of 0.3% has been imposed in the RANS. On the other hand, the wake TI is higher in the case of the LES and can reach values up to twice the RANS wake TI between 15 and 80% of the stator span (Fig. 25d). This may be

explained by the flow separation at the fan leading edge that is more significant in the LES than in the RANS, and interacts with the downstream wake, contributing to its thickening. The tip gap region is characterized by a decrease and a sudden increase in the TI, showing the interaction of the wake and the tip gap flow. For both background and wake TI, the LES unveils a sudden increase in TI near the hub and the casing. However, in the case of the RANS, this increase cannot be observed at the hub because the extrapolation process does not account for the presence of the splitter.

The different TLS estimates are plotted in Fig. 26. The radial distribution of Λ_j is very similar for both simulations, except at 15% of the stator span, where a slight decrease in the TLS, which may result from the interaction of the wake with the splitter, is observed for the LES. The values are higher for the LES because the wake width is larger than in the RANS over the whole vane span. Once again, this may be the consequence of a stronger interaction between the separated flow and the downstream wake in the LES. As expected, according to Jacob et al. [54] and Grilliat et al. [55], the same increase in Λ_j is observed near the tip gap region where the wake substantially thickens because of its interaction with the tip gap flow, which is certainly not well captured by the RANS prediction as it is highly unsteady.

The Λ_c estimate displays a quite different behavior than the Λ_j . In the background flow, Λ_c is almost constant from the hub up to 80% of the vane span with significantly larger values than those obtained for Λ_j . Near the tip, its shape is similar to the Λ_p estimate for the RANS, with a decrease in the estimated TLS as one gets closer to the casing. Similar observations were made by Leonard et al. on the SDT configuration [4]. In the wake, the Λ_c estimate provides values that are of the same order of magnitude as the LES- Λ_j estimate. However, the radial distribution of Λ_c displays pronounced differences with Jurdic's estimate. Λ_c increases from the hub up to 40% of the vane span and then decreases up to the casing. The decrease in Λ_c in the wake starts closer to the hub than in the background flow. In terms of shape, Λ_c is thus much closer to Λ_p than to Λ_j . The wake Λ_c is smaller than that in the background, which is the opposite of what is predicted by Λ_p . The unexpected larger background Λ_c may be an artifact of the postprocessing as the TLS is assessed in a region that hardly displays any turbulent features, leading to such a result.

The results obtained from Λ_c , especially the decreasing trend near the tip, question the validity of Jurdic's estimate in such a flow configuration. It seems that the flow detachment observed on the fan leading edge has significantly modified the wake structure and has led to a flow configuration that does not correspond to the one in which this estimate was observed. This result may also indicate that a finer mesh is needed in the background flow or on the blade surface, to faithfully capture the turbulent structures.

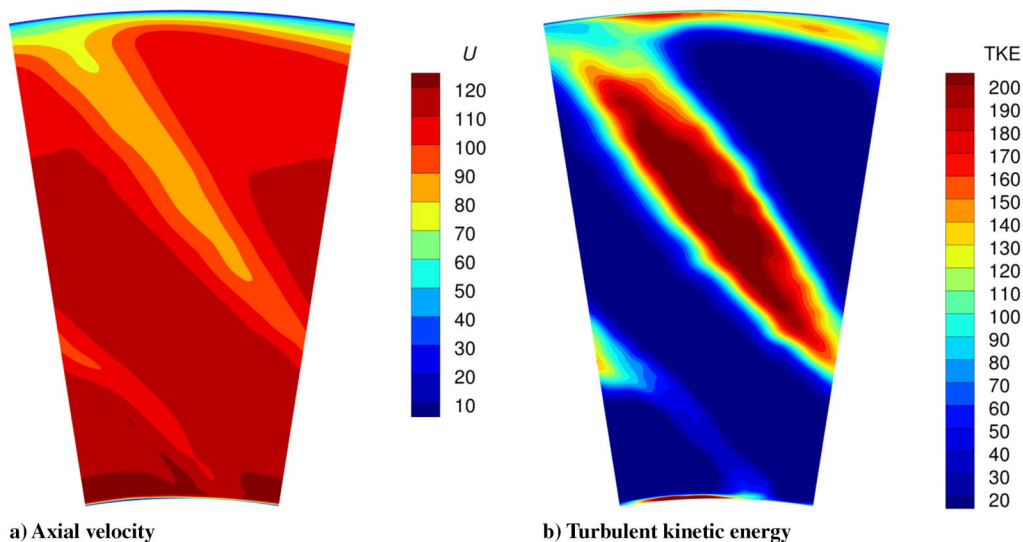


Fig. 24 Phase locked average at LE1 position.

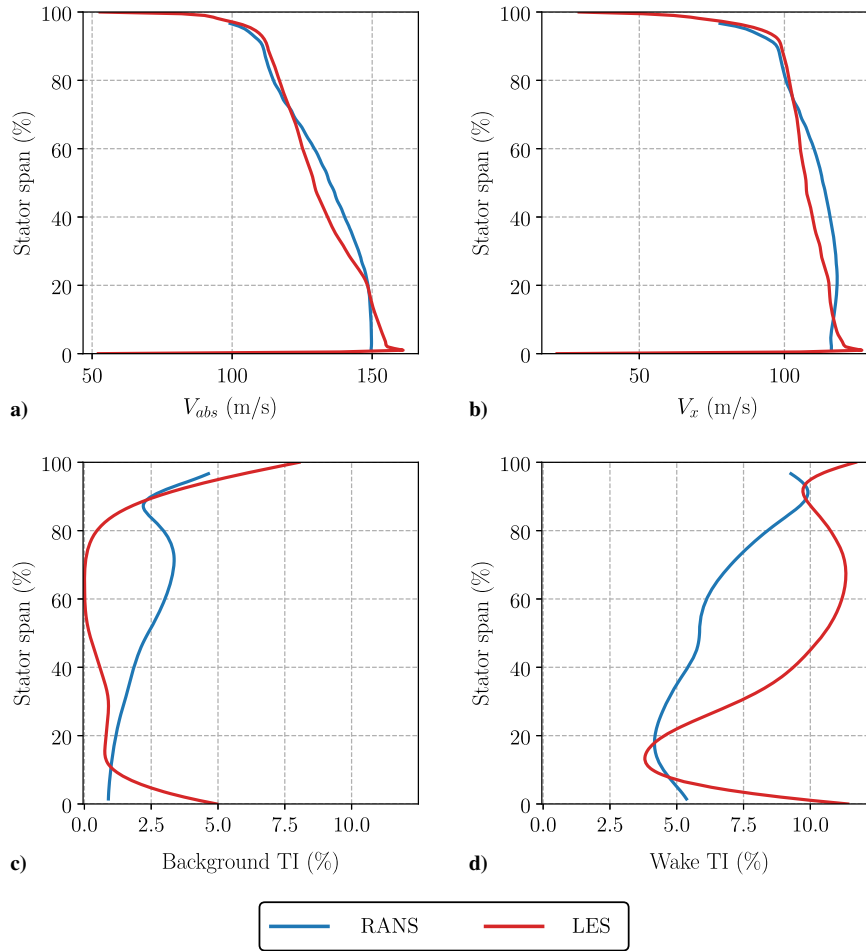


Fig. 25 Comparison of the model input parameters extracted from both RANS and LES.

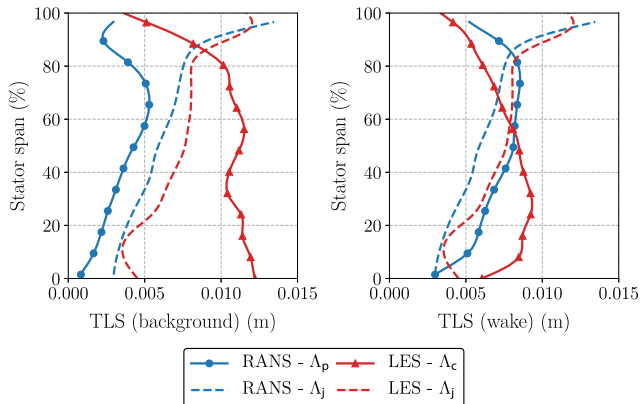


Fig. 26 Comparison of the different TLS estimates extracted from both RANS [24] and LES.

B. Analytical Model Results

Two models representing the state-of-the-art of analytical broadband RSI noise prediction have been applied: the model of Hanson [56], and the model of Posson et al. [5,7,57] as implemented in the *Optibru* platform. They are both derived from Glegg's model [58], which computes the acoustic field resulting from the interaction of a 3D incident gust with a rectilinear cascade of zero-thickness flat plates of infinite span. To account for the spanwise geometric and aerodynamic variations, they rely on the strip theory in which the stator is divided into several unwrapped radial strips, each of them corresponding to Glegg's configuration.

The main difference between the two models is the acoustic propagation method. On the one hand, Hanson's model propagates

the acoustic waves within each strip and accounts for the mean axial flow. On the other hand, Posson's model computes the vane unsteady loading, which is then used as an equivalent dipole source within an in-duct acoustic analogy that takes into account a uniform axial flow. Consequently, Posson's model considers a distribution of the acoustic energy over the duct cut-on modes, whereas Hanson's model totally neglects the duct propagation effects.

The experimental sound power levels (SWLs) displayed in the following result comparisons have been computed from the microphone measurements using different methods. The upstream SWL obtained from the forward arc was computed by integrating the sound pressure spectra measured by the far-field microphones weighted by the sine of the radiation angle. The downstream SWL was computed using the pressure signals at the casing of the bypass section by assuming a particular energy distribution over the acoustic cut-on modes. This method is referred to as wave number decomposition (WND) and is detailed by Tapken et al. [27].

Both models have been informed with the input parameters described in the previous section. Figures 27 and 28 show the prediction for both noise models using the previously discussed integral length scale estimates. The LES results have been plotted along with the RANS predictions performed by Lewis et al. [24] to get a more comprehensive analysis. Regarding the LES-informed predictions, the integral length scale estimate has a significant impact on the noise predictions for both models. Similarly to what was observed by Lewis et al. [24] and by Kissner et al. [11] for the RANS-informed predictions, the fact that the LES- Λ_j is larger than Λ_c near the casing leads to higher noise levels at low frequencies, confirming that the strips located near the casing are responsible for a significant part of the radiated noise. It should, however, be noted that the gap at low frequency between the Λ_c and LES- Λ_j predictions is several dB lower than between the Λ_p and Λ_j RANS-informed

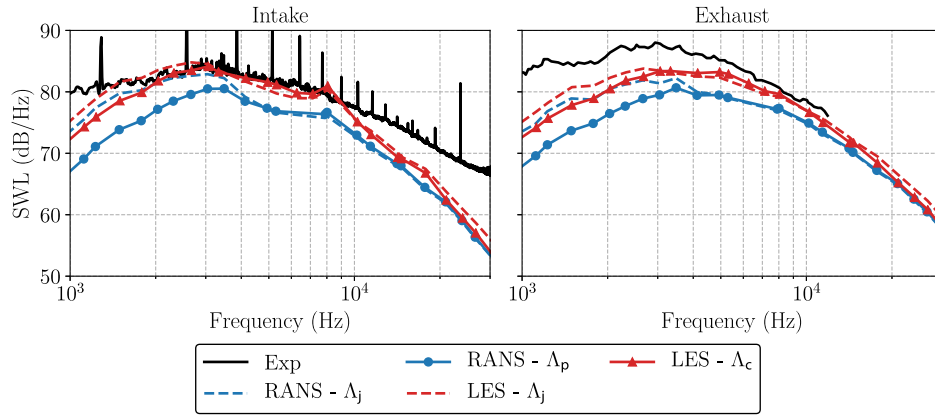


Fig. 27 Upstream SWL (left) and downstream SWL (right) spectra predicted by Posson's model.

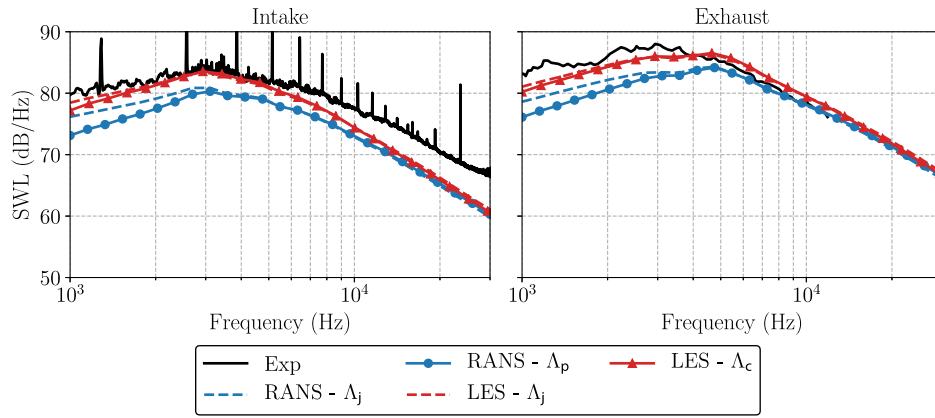


Fig. 28 Upstream SWL (left) and downstream SWL (right) spectra predicted by Hanson's model.

predictions, despite similar trends in the near-casing region. This may be due to the high Λ_c values in the lower part of the background and wake flows that could counterbalance the effect of the near-casing strips. This behavior has eventually led to a maximum low-frequency gap of 2 dB for Hanson's model and 3 dB for Posson's model between the two LES predictions. It emphasizes the paramount role of the tip flow wake, confirming the necessity to accurately simulate this region.

Despite noticeable disparities in the TLS estimates, especially in the background flow, the LES-informed predictions using the two estimates almost overlay above 5 kHz. This is particularly the case for Hanson's model. For Posson's model, the TLS disparities have had a slight impact at high-frequencies as well. Indeed, in addition to the near-casing strip effect, the TLS differences has induced a slight tilting of the spectrum, leading to an almost constant 1 dB gap above 5 kHz between the two LES predictions.

Considering only the predictions using Λ_j , it appears that the LES predictions are closer to the experimental data than the RANS-informed predictions. Similar observations were made by Leonard et al. [4] on the SDT configuration when comparing predictions from RANS and LES-informed analytical models. In the present case, an increase in the SWL by 2–4 dB is observed over the whole frequency range for the LES with respect to the RANS data. This increase results from the simultaneous increase in the wake TI and in Λ_j for the LES relatively to the RANS. To better discriminate the effect of the mean flow parameters, especially the TI, from the TLS estimate differences, predictions have been performed using Hanson's model informed with inputs consisting of a combination of the RANS mean flow parameters (axial and absolute velocities, TI profiles) and the two LES TLS estimates. In this way, only the effect of the TLS input is observed. As shown in Fig. 29, the use of the RANS TI profiles has induced a decrease in the LES-informed noise predictions by 1–2 dB over the

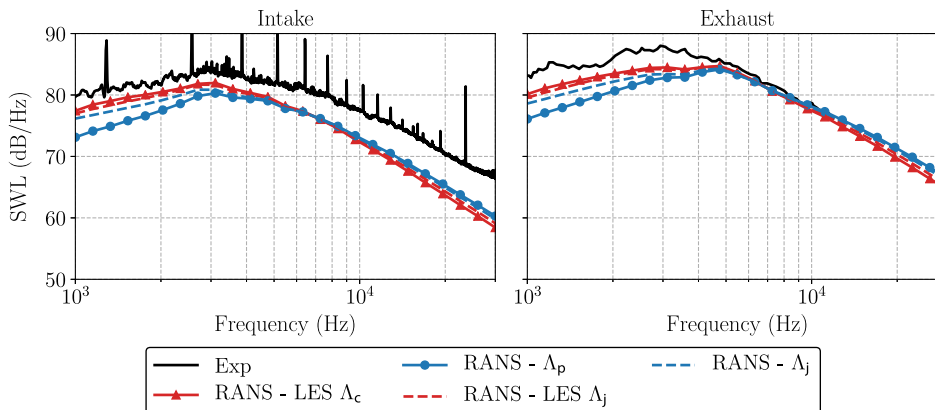


Fig. 29 Upstream SWL (left) and downstream SWL (right) spectra predicted by Hanson's model using LES TLS estimates with RANS mean flow inputs.

entire studied frequency range with respect to the full LES inputs. The TLS disparities lead to a tilting of the spectra centered around 5 kHz. Larger TLS values lead to a clockwise tilting, confirming that the larger wake and background TLS values observed in the lower part of the LES profiles are partly responsible for the low-frequency disparities observed with the RANS-informed predictions.

Figure 30 shows the direct comparison of the LES-informed predictions obtained from Hanson's and Posson's models, when using the two available TLS estimates. As with the RANS, Posson's model tends to underestimate the noise at low frequency relatively to Hanson's model. This is mainly attributed to the duct cutoff effect that has a noticeable impact, especially at low frequencies for which a major part of the first modes is cutoff. The frequency for which the maximum SWL is observed is well captured by the model of Posson for both upstream and downstream predictions when using Λ_j . Hanson's model, however, only captures the frequency of the SWL peak for the upstream prediction. When using Λ_c , the capacity to capture the frequency at the SWL peak is conserved by both models. In terms of shape, Hanson's model is closer to the upstream experimental spectrum, whereas Posson's model recovers quite faithfully the shape of the downstream experimental spectrum. This may be because Posson's model uses the inner and outer radii of the bypass section as references for the in-duct propagation, leading to a more important cutoff effect for the upstream part but to a more faithful downstream prediction. In terms of absolute levels, both models underestimate the upstream noise from medium to high frequencies, with a gap ranging from 2 to 10 dB for the highest frequencies. For the downstream prediction, Hanson's model recovers the experimental noise level, whereas an underestimation by 2–5 dB is observed for Posson's model over the whole frequency range. Posson's model predicts a balance between the upstream and downstream noise levels (as also observed by Posson et al. [7] on the SDT configuration), whereas Hanson's model predicts a higher downstream noise. The RSI mechanism usually results in a higher downstream noise, but this mainly stems from the shielding effect of the rotor [59], which is not taken into account in the present computations. It is thus surprising that such a higher downstream noise is predicted by Hanson's model, which may mean that it overestimates the upstream attenuation. Further investigation is needed to precisely understand this behavior.

As already discussed in [24], Hanson's model provides an overall better estimate of the intake and exhaust SWLs than Posson's model. Conclusions have to be drawn carefully because the duct geometry both upstream and downstream of the OGV, as well as rotor reflections are likely to impact the sound transmission. In that perspective, Posson's model better takes into account the effect of the duct on the sound propagation, because it expresses the solution as a sum of cut-on cylindrical duct modes. As a consequence, the seeming underprediction of Posson's model may actually be the most trustworthy for the RSI mechanism, which would indicate the presence of other significant noise sources in the actual experiment. As highlighted by Kholodov and Moreau [32] on the SDT configuration at approach condition, the fan tip noise, the leading-edge, and trailing-edge noise

may be interesting additional sources to consider, especially in the present case because the leading-edge flow detachment is more significant than that observed on the SDT. The fact that both models still underpredict the radiated noise in spite of the fact that the TI levels are significantly higher in the LES than in the experiment also supports this latter point.

VI. Broadband Noise Predictions Using a Hybrid Numerical Approach

A. Source Localization

The previous LES-informed analytical model approach has been performed for comparison purposes but does not represent a viable noise prediction approach given the cost of an LES. LES is in fact better suited for high-fidelity numerical hybrid methods dedicated to broadband noise predictions. This kind of method is a two-step approach that decouples the computation of the acoustic sources, performed through a scale-resolving simulation such as LES, from the propagation, usually performed through the use of an acoustic analogy. In the present case, the sources correspond to the wall pressure fluctuations on the stator surface, which have been extracted from the simulation over about four full rotor revolutions. Before performing any numerical noise predictions, it is thus of prime interest to analyze the broadband noise sources on the vane surface. A practical way to get an overview of the potential noise sources is to examine the RMS of the pressure fluctuations P_{rms} on the surface of interest. As shown in Fig. 31, high P_{rms} levels can be observed at the stator leading edge. This phenomenon is typical of the RSI mechanism and results from the impact of the turbulent rotor wakes onto the stator. A second zone of important RMS levels, starting at about 60% stator chord, can also be observed. This zone corresponds to the boundary-layer separation observed in Sec. IV.B.2, which resulted in

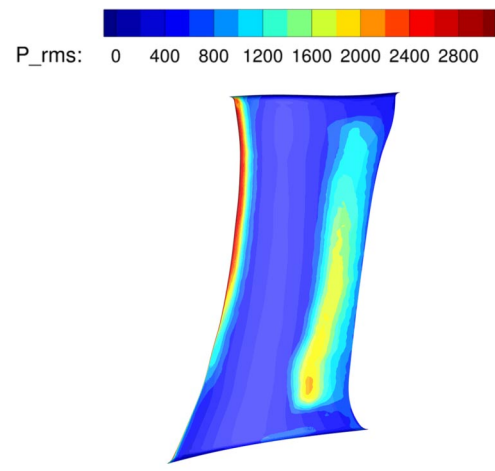


Fig. 31 P_{rms} values on the stator suction side.

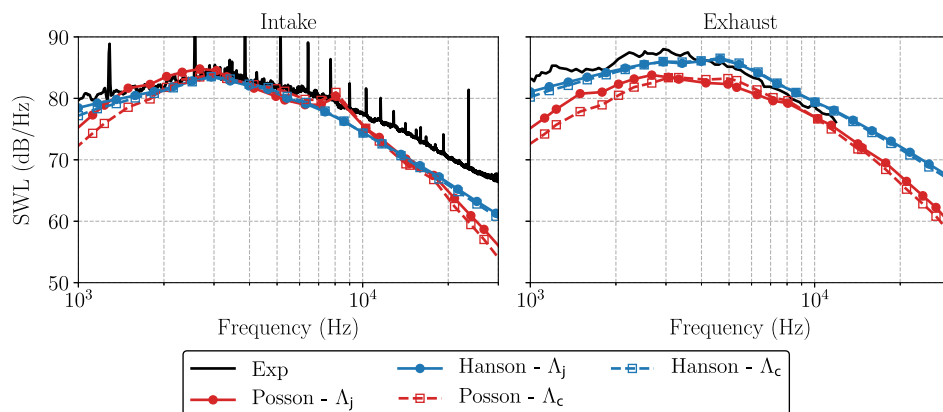


Fig. 30 Upstream SWL (left) and downstream SWL (right) spectra predicted by Hanson's and Posson's models using LES data.

intense pressure fluctuations due to the boundary-layer transition. Given that the rear-part pressure fluctuations are not negligible with respect to the leading-edge ones, they may contribute to some extent to the total radiated noise.

To have a better idea of how these fluctuations are spread over the studied frequency range, the power spectral density (PSD) of the pressure fluctuations ϕ_{pp} has been computed along the chord of the stator at 25, 50, and 75% stator span, as shown in Fig. 32. For all radial locations, the leading-edge pressure fluctuations are spread over the whole frequency range, with higher values from 1 to 8 kHz. Slightly lower levels are found at 25% stator span. The pressure fluctuations in the rear part of the OGV (60–100% of the stator chord) are the most intense between 1 and 8 kHz, indicating the creation of a wide range of turbulent structures of different sizes. Intense ϕ_{pp} levels are observed at the BPF and its harmonics over the whole vane chord because of the convection of the rotor wakes throughout the intervane channel. The sampling frequency of the signal as well as the mesh resolution lead to a wide zone of low ϕ_{pp} magnitude at high frequency.

B. Noise Predictions

The pressure fluctuations analyzed in Sec. VI.A have been used as dipole sources within the free-field FW-H analogy and Goldstein's analogy extended to annular ducts, as implemented in the tools *SherFWH* and *SherGoldstein* developed by the Aeroacoustics Group of Université de Sherbrooke [19,60]. *SherFWH* corresponds to an implementation of the formulations of Casalino [61] and Najafi-Yazdi et al. [62]. *SherGoldstein* computes the acoustic power in the upstream and downstream directions according to Eq. (5a) from [7], which makes direct use of the pressure amplitude of each annular duct mode resulting from the Fourier transform of the pressure jump through the stator vane. Further details about these tools are provided in [19]. As previously mentioned, FW-H's analogy propagates the sound in the free field, which means that the duct geometry is neglected. Moreover, extracting the sources directly on the vane surface implies that the quadrupole sources are neglected [17]. This is actually a fairly reasonable assumption because the tip relative Mach number of the rotor is 0.57, which makes it possible to neglect both monopole and quadrupole sources [17].

The pressure fluctuations on the vane have been recorded over about four rotations with a sampling frequency of 110 kHz, leading to

a Nyquist frequency of 55 kHz. The far-field SWL has been obtained using Welch's method and Hann windows with 50% overlap and 10 windows for the averaging process, which leads to a frequency resolution of $\Delta f = 282$ Hz.

Figure 33 shows the noise predictions obtained using both FW-H's and Goldstein's analogies. For both upstream and downstream predictions, the FW-H prediction recovers quite faithfully the overall shape of the experimental spectrum. In terms of absolute levels, however, a significant overprediction of the radiated noise can be observed. This is especially the case for the upstream prediction that displays a 10 dB gap from low to medium frequencies. Above 6 kHz, however, this gap decreases to 5 dB and remains constant up to higher frequencies. The overprediction of the noise for the downstream part is not as important as for the upstream one. The difference with respect to the experiment is only of 2 dB on most of the studied frequency range, except at low frequencies where it can reach 5 dB. Goldstein's analogy correctly recovers the overall shape of the experimental spectra. It provides noise levels that are at least 3 dB lower than those provided by FW-H's analogy over the entire chosen frequency range. This is especially the case at low and medium frequencies, where a 5–10 dB reduction is observed for both upstream and downstream SWL. This confirms that the overprediction observed with the FW-H analogy is partly due to the free-field propagation, which neglects the duct cutoff effect as well as the real distribution of the acoustic energy over the duct modes. The noise reduction resulting from the duct effect is of the same order as that estimated on the NASA SDT configuration by Pérez Arroyo et al. [19], who observed a 5–10 dB reduction of the predicted noise over the whole frequency range with respect to the FW-H-based prediction. Despite the fact that Goldstein's analogy provides noise estimates closer to the measurements, a significant overestimation of the noise is still observed, especially upstream of the OGV.

Furthermore, as mentioned in Sec. IV.B.2, a flow detachment occurs in the rear part of the stator vane, which was not observed in the RANS study. This flow separation, if not well predicted, may be partly responsible for the remaining overprediction. To assess how significant its contribution to the radiated noise is, the vane has been split in two parts: the front part, consisting of the first 40% of the vane maximum axial chord over the entire vane span, and the aft part, which consists of the 60% left. Considering this splitting, the PSD Γ_{full} induced by the pressure fluctuations on the full blade at a

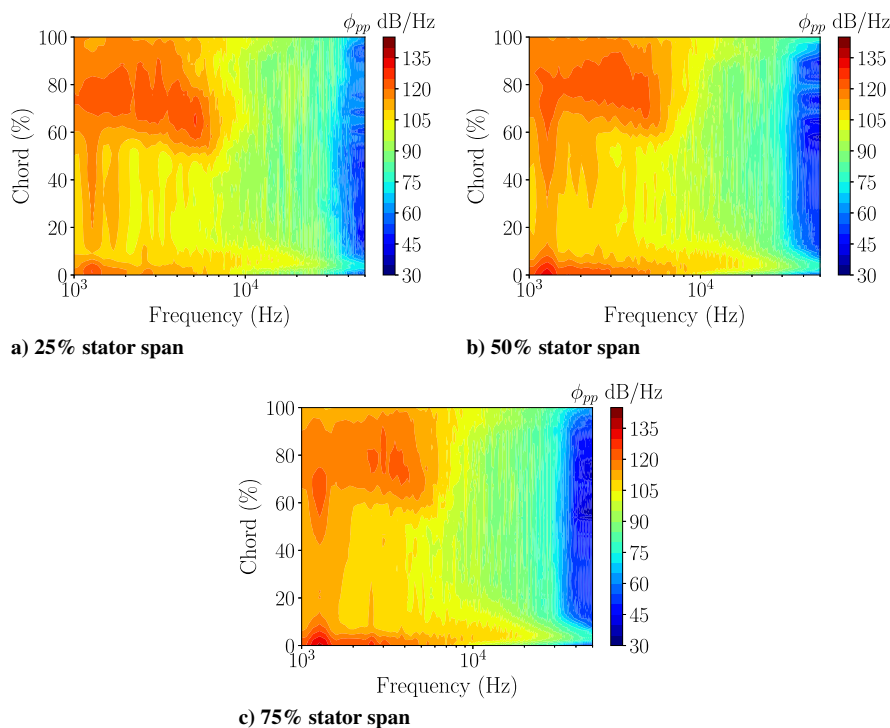


Fig. 32 PSD of the pressure fluctuations on the stator surface at different radial positions.

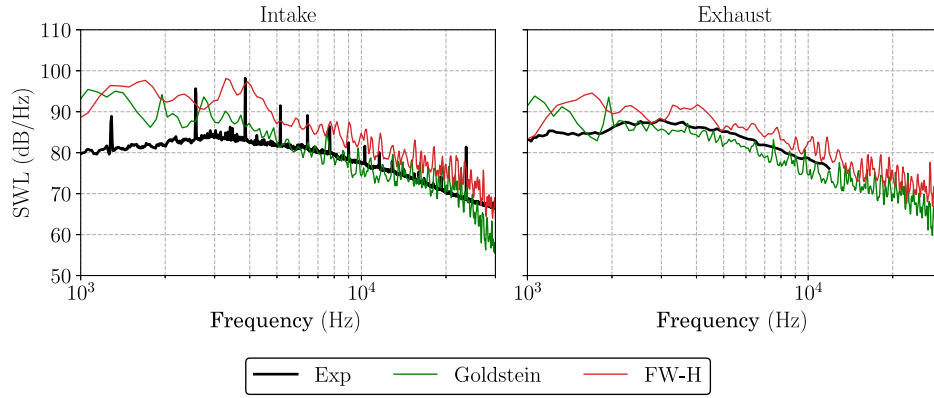


Fig. 33 Upstream SWL (left) and downstream SWL (right) spectra obtained from FW-H’s and Goldstein’s analogies.

particular observer point can be rewritten as follows:

$$\Gamma_{full} = \Gamma_{Front} + \Gamma_{Aft} + 2Re(\Gamma_{Front,Aft}) \quad (8)$$

where Γ_{Front} and Γ_{Aft} are the PSD induced by the front and the aft parts of the vane respectively, $\Gamma_{Front,Aft}$ is the cross-spectral density between the front and the aft signals (corresponding to the Fourier transform of the cross-correlation function), and $Re()$ denotes the real part of the quantity in parentheses. These three terms (Γ_{Front} , Γ_{Aft} , and $2Re(\Gamma_{Front,Aft})$) have been computed separately and plotted along with the full-vane-based prediction, which was computed using the entire OGV surface, in Fig. 34. The noise estimates based on the split vane subparts could only be performed with the FW-H analogy as this feature is yet to be implemented in *SherGoldstein*.

As it can be seen, the aft part of the vane is responsible for most of the noise radiated by the vane, which means that in the present computation, the noise due to the flow separation might be more important than expected. Moreover, the fact that the front and the cross terms display noise levels similar to or lower than those observed in the experiment may indicate that the observed rear flow separation is less important in the experiment, and that it could be a consequence of a lack of mesh refinements on the vane surface. Further investigation is needed to precisely determine to which extent this flow separation contributes to the total radiated noise. The cross-spectra also show that the upstream and aft part of the vane pressure fluctuations are correlated, indicating a possible downstream shift of the RSI sources.

Two other chordwise splitting locations have also been investigated: a splitting at 50% maximum axial chord (see Fig. 35), and

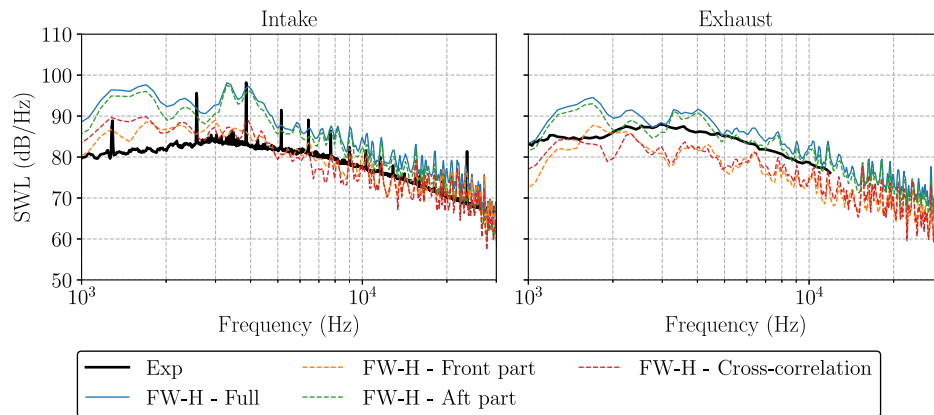


Fig. 34 Upstream SWL (left) and downstream SWL (right) spectra obtained from FW-H’s analogy. Chordwise separation at 40% maximum axial chord.

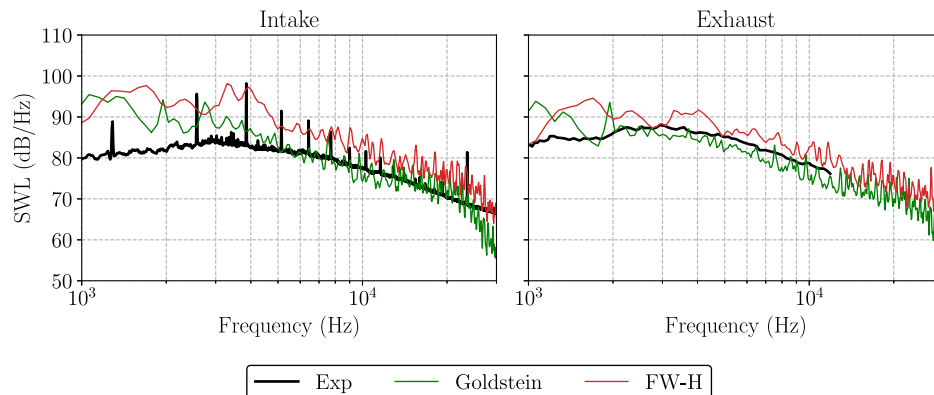


Fig. 35 Upstream SWL (left) and downstream SWL (right) spectra obtained from FW-H’s analogy. Chordwise splitting at 50% maximum axial chord.

another at 60% maximum axial chord (see Fig. 36). Regarding the 50% splitting, the three noise components have much more similar levels than with the 40% splitting. The aft part remains the major contributor to the total noise over most of the studied frequency range, whether in the downstream or upstream direction. This trend, however, changes for the 60% splitting, for which the front part contributes the most to the total noise as it encompasses part of the fluctuations generated by the rear flow detachment. The gap between the front and the aft part noise is, however, much smaller than that observed for the 40% splitting, confirming the substantial contribution of the aft part of the OGV to the overall noise.

To assess the consistency between the analytical and the numerical predictions, the FW-H prediction based on the first 40% of the vane maximum axial chord has been plotted along with the predictions using Hanson's model in Fig. 37. The 40% FW-H prediction has been selected for the comparison because it presumably encompasses only the RSI sources. Part of the RSI sources might, however, have been truncated with this process because the previous discussions revealed that a rigorous splitting of the different sources is difficult. This may result in a ± 2 dB uncertainty. Hanson's model was chosen for the comparisons because it is the closest to the FW-H analogy in terms of modeling assumptions. For the upstream noise, the FW-H predictions and both analytical LES-informed predictions provide comparable estimates at medium and high frequency. More significant disparities appear at low frequency when considering the RANS-informed predictions. As shown in Sec. V.B, this is partly the consequence of the lower TI observed in the RANS simulation. For the downstream noise, the FW-H prediction and the LES-informed analytical predictions provide similar noise levels at low frequency, whereas a 4–8 dB discrepancy appears at medium and high frequency. This essentially stems from the fact that the upstream/downstream SWL-predicted balance is different in the present case for analytical and numerical computations: Hanson's model predicts a downstream

noise that is higher than the upstream one, whereas the FW-H analogy predicts the opposite. As already discussed in Sec. V.B, the higher downstream noise usually observed when studying the RSI mechanism actually stems from the shielding effect of the rotor [59], which is not taken into account in the present computations. It is thus surprising that Hanson's model predicts such a different upstream/downstream balance with respect to the FW-H analogy. Further investigation is needed to better explain this point.

VII. Conclusions

A comprehensive noise computation of the ACAT1 configuration at approach condition has been performed using a medium-sized mesh LES that meets the requirement for wall-modeled simulations. The LES is in good agreement with the experimental performance parameters and with the mean velocity profiles retrieved from the HW measurements, exhibiting only small discrepancies within the experimental uncertainty for the latter. RMS levels are, however, significantly overestimated by the simulation, which can be partly explained by the underestimation of the experimental RMS levels resulting from the thickness of the HWs. Two hybrid noise computation methods have been used. The first is the LES-informed analytical model approach. The impact of the two available turbulence length scale estimates on the SWL has been studied, showing that a higher low-frequency noise is observed when using Jurdic's estimate due to the larger TLS values it predicts near the casing. This effect is, however, less important than for the corresponding RANS-informed study [24] because of the larger background and wake TLS outside of the tip region, which seems to have counterbalanced it. Both Hanson's and Posson's models underestimate the noise levels on a large part of the studied frequency range, with noise levels closer to the experiment in the case of Hanson's model mainly because it neglects the duct cutoff effect. This underestimation may indicate the presence

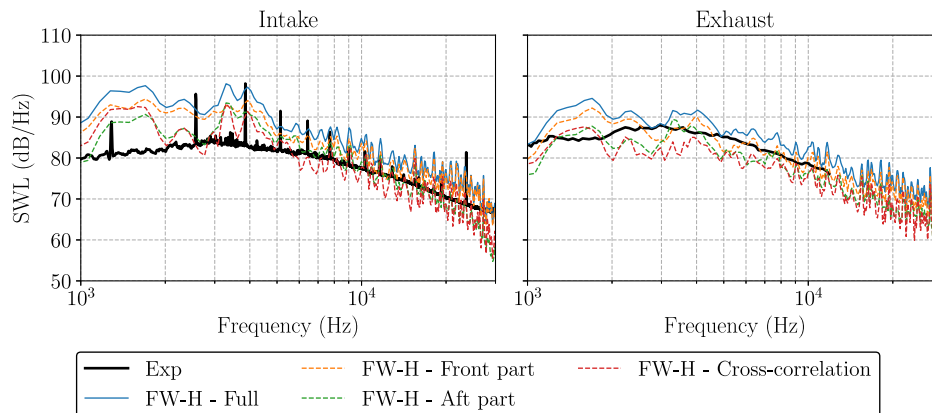


Fig. 36 Upstream SWL (left) and downstream SWL (right) spectra obtained from FW-H's analogy. Chordwise splitting at 60% maximum axial chord.

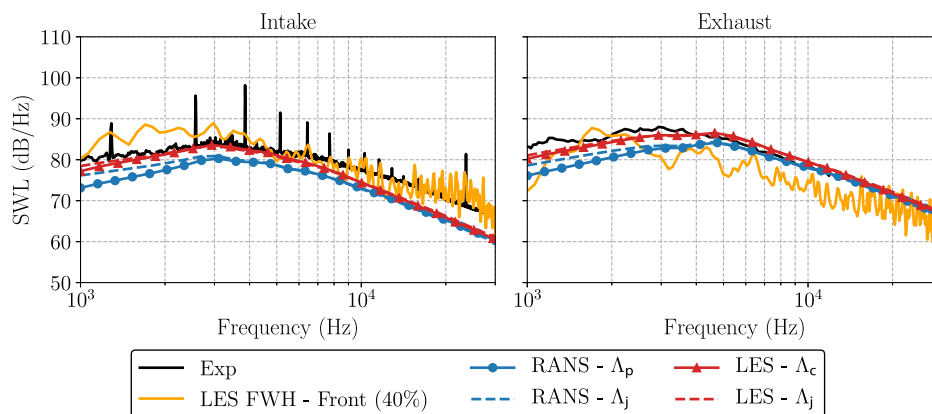


Fig. 37 Upstream SWL (left) and downstream SWL (right) spectra obtained from FW-H's analogy (front part noise only with 40% splitting) and from the analytical predictions using Hanson's model.

of additional noise sources in the experiment, which may not be negligible with respect to the RSI mechanism.

A high-fidelity hybrid approach, coupling the LES with both FW-H's analogy and Goldstein's analogy extended to annular ducts, has then been applied to assess the noise radiated by the stator row. A global overestimation of the radiated noise is observed when resorting to FW-H's analogy, especially for the upstream prediction, which reveals discrepancies with the experiment that can reach 10 dB at low frequencies. Part of this overestimation is attributed to the fact that the FW-H analogy neglects the duct propagation effect. The use of Goldstein's analogy has reduced this overprediction by 3–10 dB, but has still resulted in overestimated noise levels especially in the upstream direction. Moreover, it seems that the vane flow separation contributes more significantly than expected to the overall noise with respect to the RSI mechanism, which may indicate a need to refine the wall mesh in this zone to guarantee that it is well captured.

Further investigation using a finer mesh is needed to confirm the presence of some flow features such as the flow separation on the stator vane. Such a study would shed light on the noise underprediction observed when using LES-informed analytical models despite an overpredicted turbulence, but also on the overestimated noise predicted by the FW-H analogy. The fact that the selected operating point is close to surge might also induce some instabilities in the flow that make the prediction of flow detachments more arduous, especially when using wall-modeling. This study also revealed that the RSI mechanism may not be the only dominant broadband noise source and that additional sources such as the rotor leading-edge flow detachment may significantly contribute to the radiated noise.

Acknowledgments

The presented work was conducted in the framework of the project TurboNoiseBB, which has received funding from the European Union's Horizon 2020 research and innovation program under grant agreement number 690714. This work was performed within the framework of the LABEX CeLyA (ANR-10-LABX-0060) of Université de Lyon, within the program "Investissements d'Avenir" (ANR-16-IDEX-0005) operated by the French National Research Agency (ANR). The computational resources were provided by the GENCI network (CINES-OCCIGEN, project number A0062A0 6074), by CERFACS, and by PMCS21-FLMSN. The authors want to thank the members of the TurboNoiseBB consortium for providing experimental data and for fruitful discussions throughout the project. The authors also want to thank Raphaël Barrier (ONERA) for providing the rescaled outlet guide vane. Marlène Sanjosé's contribution to this work essentially consisted in developing and providing the Goldstein analogy (i.e. the FW-H analogy formulated in an annular duct). M. Sanjosé also provided guidelines about the application of this analogy. In this context, the numerous discussions with P. Khodolov (UdS) on the subtleties of the Goldstein formulation were also of great interest. The authors want to thank Nicolas Odier and Maxime Fiore from CERFACS for their many pieces of advice on the meshing process and for the fruitful conversations on the use of AVBP and on the large-eddy simulation (LES) postprocessing. The help from Florent Duchaine (CERFACS) for the application to obtain computational resources on GENCI's cluster was also greatly appreciated. Most of the LES postprocessing was performed using Antares (release 1.15.0, <https://www.cerfacs.fr/antares>).

References

- [1] Moreau, S., "Turbomachinery Noise Predictions: Present and Future," *Acoustics*, Vol. 1, No. 1, 2019, pp. 92–116. <https://doi.org/10.3390/acoustics1010008>
- [2] Moreau, S., and Roger, M., "Advanced Noise Modeling for Future Propulsion Systems," *International Journal of Aeroacoustics*, Vol. 17, Nos. 6–8, 2018, pp. 576–599. <https://doi.org/10.1177/1475472X18789005>
- [3] Peake, N., and Parry, A. B., "Modern Challenges Facing Turbomachinery Aeroacoustics," *Annual Review of Fluid Mechanics*, Vol. 44, Jan. 2012, pp. 227–248. <https://doi.org/10.1146/annurev-fluid-120710-101231>
- [4] Leonard, T., Sanjose, M., Moreau, S., and Duchaine, F., "Large Eddy Simulation of a Scale-Model Turbofan for Fan Noise Source Diagnostic," *22nd AIAA/CEAS Aeroacoustics Conference*, AIAA Paper 2016-3000, 2016. <https://doi.org/10.2514/6.2016-3000>
- [5] Posson, H., Moreau, S., and Roger, M., "On the Use of a Uniformly Valid Analytical Cascade Response Function for Fan Broadband Noise Predictions," *Journal of Sound and Vibration*, Vol. 329, No. 18, 2010, pp. 3721–3743. <https://doi.org/10.1016/j.jsv.2010.03.009>
- [6] Masson, V., Posson, H., Sanjose, M., Léonard, T., Moreau, S., and Roger, M., "Fan-OGV Interaction Broadband Noise Prediction in a Rigid Annular Duct with Swirling and Sheared Mean Flow," *22nd AIAA/CEAS Aeroacoustics Conference*, AIAA Paper 2016-2944, 2016. <https://doi.org/10.2514/6.2016-2944>
- [7] Posson, H., Moreau, S., and Roger, M., "Broadband Noise Prediction of Fan Outlet Guide Vane Using a Cascade Response Function," *Journal of Sound and Vibration*, Vol. 330, No. 25, 2011, pp. 6153–6183. <https://doi.org/10.1016/j.jsv.2011.07.040>
- [8] Grace, S., Gonzalez-Martino, I., and Casalino, D., "Analysis of Fan-Stage Gap-Flow Data to Inform Simulation of Fan Broadband Noise," *Philosophical Transactions of the Royal Society A*, Vol. 377, No. 2159, 2019, Paper 20190080. <https://doi.org/10.1098/rsta.2019.0080>
- [9] Grace, S. M., "Fan Broadband Interaction Noise Modeling Using a Low-Order Method," *Journal of Sound and Vibration*, Vol. 346, No. 1, 2015, pp. 402–423. <https://doi.org/10.1016/j.jsv.2015.02.013>
- [10] Grace, S. M., Gonzalez-Martino, I., and Casalino, D., "Analysis of Fan-Stage Gap Flow Data Generated Using an LBM/VLES Method," *25th AIAA/CEAS Aeroacoustics Conference*, AIAA Paper 2019-2668, 2019. <https://doi.org/10.2514/6.2019-2668>
- [11] Kissner, C., Guérin, S., Seeler, P., Billson, M., Paruchuri, C., Carrasco Laraña, P., de Laborde, H., François, B., Lefarth, K., Lewis, D., Montero Villar, G., and Nodé-Langlois, T., "ACAT1 Benchmark of RANS-Informed Analytical Methods for Fan Broadband Noise Prediction: Part I—Influence of the RANS Simulation," *Acoustics*, Vol. 2, No. 3, 2020, pp. 539–578. <https://doi.org/10.3390/acoustics2030029>
- [12] Guerin, S., Kissner, C. A., Kajasa, B., Jaron, R., Behn, M., Pardowitz, B., Tapken, U., Hakansson, S., Meyer, R., and Enghardt, L., "Noise Prediction of the ACAT1 Fan with a RANS-Informed Analytical Method: Success and Challenge," *25th AIAA/CEAS Aeroacoustics Conference*, AIAA Paper 2019-2500, 2019. <https://doi.org/10.2514/6.2019-2500>
- [13] Guerin, S., Kissner, C., Seeler, P., Blazquez Navarro, R. A., Carrasco Laraña, P., de Laborde, H., Lewis, D., Paruchuri, C., and Polacsek, C., "ACAT1 Benchmark of RANS-Informed Analytical Methods for Fan Broadband Noise Prediction: Part II—Influence of the Acoustic Models," *Acoustics*, Vol. 2, No. 3, 2020, pp. 617–649. <https://doi.org/10.3390/acoustics2030033>
- [14] Polacsek, C., Daroukh, M., François, B., and Barrier, R., "Turbofan Broadband Noise Predictions Based on a ZDES Calculation of a Fan-OGV Stage," *9th Forum Acusticum*, European Acoustics Association (EAA), Spain, 2020. <https://doi.org/10.48465/fa.2020.0032>
- [15] Nallasamy, M., and Envía, E., "Computation of Rotor Wake Turbulence Noise," *Journal of Sound and Vibration*, Vol. 282, Nos. 3–5, 2005, pp. 649–678. <https://doi.org/10.1016/j.jsv.2004.03.062>
- [16] Jurdic, V., Moreau, A., Joseph, P., Enghardt, L., and Coupland, J., "A Comparison Between Measured and Predicted Fan Broadband Noise due to Rotor-Stator Interaction," *13th AIAA/CEAS Aeroacoustics Conference*, AIAA Paper 2007-3692, 2007. <https://doi.org/10.1016/j.jsv.2004.03.062>
- [17] Ffowcs Williams, J. E., and Hawkings, D. L., "Sound Generation by Turbulence and Surfaces in Arbitrary Motion," *Philosophical Transactions of the Royal Society of London. Series A, Mathematical and Physical Sciences*, Vol. 264, No. 1151, 1969, pp. 321–342. <https://doi.org/10.1098/rsta.1969.0031>
- [18] Goldstein, M. E., *Aeroacoustics*, McGraw-Hill, New York, 1976, p. 305.
- [19] Pérez Arroyo, C., Leonard, T., Sanjosé, M., Moreau, S., and Duchaine, F., "Large Eddy Simulation of a Scale-Model Turbofan for Fan Noise Source Diagnostic," *Journal of Sound and Vibration*, Vol. 445, April 2019, pp. 64–76. <https://doi.org/10.1016/j.jsv.2019.01.005>
- [20] Gonzalez-Martino, I., and Casalino, D., "Fan Tonal and Broadband Noise Simulations at Transonic Operating Conditions Using Lattice-Boltzmann Methods," *24th AIAA/CEAS Aeroacoustics Conference*,

- AIAA Paper 2018-3919, 2018.
<https://doi.org/10.2514/6.2018-3919>
- [21] Casalino, D., Hazir, A., and Mann, A., "Turbofan Broadband Noise Prediction Using the Lattice Boltzmann Method," *AIAA Journal*, Vol. 56, No. 2, 2018, pp. 609–628.
<https://doi.org/10.2514/1.J055674>
- [22] Casalino, D., Ribeiro, A. F., Fares, E., Noelting, S. E., Mann, A., Perot, F., Li, Y., Lew, P.-T., Sun, C., Gopalakrishnan, P., and Zhang, R., "Towards Lattice-Boltzmann Prediction of Turbofan Engine Noise," *20th AIAA/CEAS Aeroacoustics Conference*, AIAA Paper 2014-3101, 2014.
<https://doi.org/10.2514/6.2014-3101>
- [23] Moreau, S., "A Review of Turbomachinery Noise: From Analytical Models to High-Fidelity Simulations," *Fundamentals of High Lift for Future Civil Aircraft*, Springer, Berlin, 2020, pp. 579–595, Chap. 10.
https://doi.org/10.1007/978-3-030-52429-6_35
- [24] Lewis, D., Moreau, S., and Jacob, M. C., "On the Use of RANS-Informed Analytical Models to Perform Broadband Rotor-Stator Interaction Noise Predictions," *25th AIAA/CEAS Aeroacoustics Conference*, AIAA Paper 2019-2667, 2019.
<https://doi.org/10.2514/6.2019-2667>
- [25] Meyer, R., Hakansson, S., Hage, W., and Enghardt, L., "Instantaneous Flow Field Measurements in the Interstage Section Between a Fan and the Outlet Guiding Vanes at Different Axial Positions," *Proceedings of 13th European Conference on Turbomachinery Fluid Dynamics and Thermodynamics*, Paper ETC2019-330, European Turbomachinery Soc. (Euroturbo), Italy, 2019, pp. 8–12.
<https://doi.org/10.29008/ETC2019-330>
- [26] Behn, M., and Tapken, U., "Investigation of Sound Generation and Transmission Effects Through the ACAT1 Fan Stage Using Compressed Sensing-Based Mode Analysis," *25th AIAA/CEAS Aeroacoustics Conference*, AIAA Paper 2019-2502, 2019.
<https://doi.org/10.2514/6.2019-2502>
- [27] Tapken, U., Behn, M., Spitalny, M., and Pardowitz, B., "Radial Mode Breakdown of the ACAT1 Fan Broadband Noise Generation in the Bypass Duct Using a Sparse Sensor Array," *25th AIAA/CEAS Aeroacoustics Conference*, AIAA Paper 2019-2525, 2019.
<https://doi.org/10.2514/6.2019-2525>
- [28] Brouwer, H., and Sijsma, P., "Phased Array Beamforming to Identify Broadband Noise Sources in the Interstage Section of a Turbofan Engine," *25th AIAA/CEAS Aeroacoustics Conference*, AIAA Paper 2019-2669, 2019.
<https://doi.org/10.2514/6.2019-2669>
- [29] Rai, M. M., and Madavan, N. K., "Multi-Airfoil Navier–Stokes Simulations of Turbine Rotor–Stator Interaction," *Journal of Turbomachinery*, Vol. 112, No. 3, 1990, pp. 377–384.
<https://doi.org/10.1115/1.2927670>
- [30] François, B., Barrier, R., and Polacsek, C., "Zonal Detached Eddy Simulation of the Fan-OGV Stage of a Modern Turbofan Engine," *ASME Turbo Expo: Power for Land, Sea, and Air*, Vol. 2A, American Soc. of Mechanical Engineers, 2020.
<https://doi.org/10.1115/GT2020-14239>
- [31] Odier, N., Duchaine, F., Gicquel, L., Staffelbach, G., Thacker, A., García Rosa, N., Dufour, G., and Muller, J.-D., "Evaluation of Integral Turbulence Scale Through the Fan Stage of a Turbofan Using Hot Wire Anemometry and Large Eddy Simulation," *ASME Turbo Expo: Power for Land, Sea, and Air*, Vol. 2C, American Soc. of Mechanical Engineers, 2018.
<https://doi.org/10.1115/GT2018-75741>
- [32] Kholodov, P., and Moreau, S., "Identification of Noise Sources in a Realistic Turbofan Rotor Using Large Eddy Simulation," *Acoustics*, Vol. 2, No. 3, 2020, pp. 691–706.
<https://doi.org/10.3390/acoustics2030037>
- [33] Kholodov, P., Pérez Arroyo, C., Sanjosé, M., and Moreau, S., "Fan Broadband Noise Computation at Transonic Regime," *25th AIAA/CEAS Aeroacoustics Conference*, AIAA Paper 2019-2714, 2019.
<https://doi.org/10.2514/6.2019-2714>
- [34] Piomelli, U., "Large Eddy Simulations in 2030 and Beyond," *Philosophical Transactions of the Royal Society A: Mathematical, Physical and Engineering Sciences*, Vol. 372, No. 2022, 2014, Paper 20130320.
<https://doi.org/10.1098/rsta.2013.0320>
- [35] Wagner, C., Hüttl, T., and Sagaut, P., *Large-Eddy Simulation for Acoustics*, Vol. 20, Cambridge Aerospace Series, Cambridge Univ. Press, 2007, Chap. 5.
<https://doi.org/10.1017/CBO9780511546143>
- [36] Schönfeld, T., and Rudgyard, M., "Steady and Unsteady Flow Simulations Using the Hybrid Flow Solver AVBP," *AIAA Journal*, Vol. 37, No. 11, 1999, pp. 1378–1385.
<https://doi.org/10.2514/2.636>
- [37] Wang, G., Duchaine, F., Papadogiannis, D., Duran, I., Moreau, S., and Gicquel, L. Y., "An Overset Grid Method for Large Eddy Simulation of Turbomachinery Stages," *Journal of Computational Physics*, Vol. 274, Oct. 2014, pp. 333–355.
<https://doi.org/10.1016/j.jcp.2014.06.006>
- [38] Lax, P. D., and Wendroff, B., "Difference Schemes for Hyperbolic Equations with High Order of Accuracy," *Communications on Pure and Applied Mathematics*, Vol. 17, No. 3, 1964, pp. 381–398.
<https://doi.org/10.1002/cpa.3160170311>
- [39] Nicoud, F., and Ducros, F., "Subgrid-Scale Stress Modelling Based on the Square of the Velocity Gradient Tensor," *Flow, Turbulence and Combustion*, Vol. 62, No. 3, 1999, pp. 183–200.
<https://doi.org/10.1023/A:1009995426001>
- [40] Poinso, T. J., and Lele, S., "Boundary Conditions for Direct Simulations of Compressible Viscous Flows," *Journal of Computational Physics*, Vol. 101, No. 1, 1992, pp. 104–129.
[https://doi.org/10.1016/0021-9991\(92\)90046-2](https://doi.org/10.1016/0021-9991(92)90046-2)
- [41] Odier, N., Sanjosé, M., Gicquel, L., Poinso, T., Moreau, S., and Duchaine, F., "A Characteristic Inlet Boundary Condition for Compressible, Turbulent, Multispecies Turbomachinery Flows," *Computers & Fluids*, Vol. 178, Jan. 2019, pp. 41–55.
<https://doi.org/10.1016/j.compfluid.2018.09.014>
- [42] Nicoud, E., Colin, O., Angelberger, C., Nicolle, F., and Krüger, C., "A No-Slip Implementation of a Wall Law Boundary Condition in a Cell-Vertex Code for LES of Internal Aerodynamics on Unstructured Meshes," *Conference LES4ICE*, IFP Energies Nouvelles, Rueil-Malmaison, 2016.
- [43] Schmitt, P., Poinso, T., Schuermans, B., and Geigle, K., "Large-Eddy Simulation and Experimental Study of Heat Transfer, Nitric Oxide Emissions and Combustion Instability in a Swirled Turbulent High-Pressure Burner," *Journal of Fluid Mechanics*, Vol. 570, Jan. 2007, pp. 17–46.
<https://doi.org/10.1017/S0022112006003156>
- [44] Wang, G., Moreau, S., Duchaine, F., De Laborderie, J., and Gicquel, L., "LES Investigation of Aerodynamics Performance in an Axial Compressor Stage," *22nd Annual Conference of the CFD Society of Canada*, Computational Fluid Dynamics Soc. of Canada, Toronto, Canada, June 2014.
- [45] Wang, G., Moreau, S., Duchaine, F., Gourdain, N., and Gicquel, L., "Large Eddy Simulations of the MT1 High-Pressure Turbine Using TurboAVBP," *Proceeding of 21st Annual Conference of the CFD Society of Canada*, Computational Fluid Dynamics Soc. of Canada, Canada, 2013, pp. 70–106.
- [46] Mockett, C., Knacke, T., and Thiele, F., "Detection of Initial Transient and Estimation of Statistical Error in Time-Resolved Turbulent Flow Data," *8th International ERCOFTAC Symposium on Engineering Turbulence Modelling and Measurements*, European Research Collaboration on Flow Turbulence and Combustion, Belgium, June 2010.
- [47] Pérez Arroyo, C., Leonard, T., Sanjosé, M., Moreau, S., and Duchaine, F., "Large Eddy Simulation of a Rotor Stage for Fan Noise Source Diagnostic," *Proceedings of the Global Power and Propulsion Forum*, Paper GPPS-NA-2018-0008, Global Power and Propulsion Soc., Switzerland, 2018, pp. 7–9, <https://pdfs.semanticscholar.org/d8cb/d363906249e6c93318cdae6edf0485916.pdf>.
- [48] Tucker, P. G., and Wang, Z.-N., "Eddy Resolving Strategies in Turbomachinery and Peripheral Components," *Journal of Turbomachinery*, Vol. 143, No. 1, 2021, Paper 010801.
<https://doi.org/10.1115/1.4048697>
- [49] Maunus, J., Grace, S., and Sondak, D., "Effect of CFD Wake Prediction in a Hybrid Simulation of Fan Broadband Interaction Noise," *17th AIAA/CEAS Aeroacoustics Conference (32nd AIAA Aeroacoustics Conference)*, AIAA Paper 2011-2875, 2011.
<https://doi.org/10.2514/6.2011-2875>
- [50] Perot, F., Moreau, S., Kim, M.-S., Henner, M., and Neal, D., "Direct Aeroacoustics Predictions of a Low Speed Axial Fan," *16th AIAA/CEAS Aeroacoustics Conference*, AIAA Paper 2010-3887, 2010.
<https://doi.org/10.2514/6.2010-3887>
- [51] Pope, S. B., *Turbulent Flows*, Cambridge Univ. Press, Cambridge, 2000, Chap. 3.
<https://doi.org/10.1017/CBO9780511840531>
- [52] Jurdic, J., Joseph, P., and Antoni, J., "Investigation of Rotor Wake Turbulence Through Cyclostationary Spectral Analysis," *AIAA Journal*, Vol. 47, No. 9, 2009, pp. 2022–2030.
<https://doi.org/10.2514/1.36728>
- [53] Jaron, R., Moreau, A., and Guerin, S., "RANS-Informed Fan Noise Prediction: Separation and Extrapolation of Rotor Wake and Potential Field," *20th AIAA/CEAS Aeroacoustics Conference*, AIAA Paper 2014-2946, 2014.
<https://doi.org/10.2514/6.2014-2946>
- [54] Jacob, M. C., Jondeau, E., and Li, B., "Time-Resolved PIV Measurements of a Tip Leakage Flow," *International Journal of Aeroacoustics*,

- Vol. 15, Nos. 6–7, 2016, pp. 662–685.
<https://doi.org/10.1177/1475472X16659384>
- [55] Grilliat, J., Jacob, M., Camussi, R., and Caputi-Gennaro, G., “Tip Leakage Experiment-Part One: Aerodynamic and Acoustic Measurements,” *13th AIAA/CEAS Aeroacoustics Conference*, AIAA Paper 2007-3684, 2007.
<https://doi.org/10.2514/6.2007-3684>
- [56] Hanson, D. B., “Theory for Broadband Noise of Rotor and Stator Cascades with Inhomogeneous Inflow Turbulence Including Effects of Lean and Sweep,” NASA CR-2001-210762, 2001.
- [57] Posson, H., Roger, M., and Moreau, S., “On a Uniformly Valid Analytical Rectilinear Cascade Response Function,” *Journal of Fluid Mechanics*, Vol. 663, Nov. 2010, pp. 22–52.
<https://doi.org/10.1017/S0022112010003368>
- [58] Glegg, S. A., “The Response of a Swept Blade Row to a Three-Dimensional Gust,” *Journal of Sound and Vibration*, Vol. 227, No. 1, 1999, pp. 29–64.
<https://doi.org/10.1006/jsvi.1999.2327>
- [59] Blázquez, R., and Corral, R., “Prediction of Fan Acoustic Blockage on Fan/Outlet Guide Vane Broadband Interaction Noise Using Efficient Frequency Domain Linearised Navier-Stokes Solvers,” *Journal of Sound and Vibration*, Vol. 500, May 2021, Paper 116033.
<https://doi.org/10.1016/j.jsv.2021.116033>
- [60] Fosso Pouangué, A., Sanjosé, M., Moreau, S., Daviller, G., and Deniau, H., “Subsonic Jet Noise Simulations Using Both Structured and Unstructured Grids,” *AIAA Journal*, Vol. 53, No. 1, 2015, pp. 55–69.
<https://doi.org/10.2514/1.J052380>
- [61] Casalino, D., “An Advanced Time Approach for Acoustic Analogy Predictions,” *Journal of Sound and Vibration*, Vol. 261, No. 4, 2003, pp. 583–612.
[https://doi.org/10.1016/S0022-460X\(02\)00986-0](https://doi.org/10.1016/S0022-460X(02)00986-0)
- [62] Najafi-Yazdi, A., Brès, G. A., and Mongeau, L., “An Acoustic Analogy Formulation for Moving Sources in Uniformly Moving Media,” *Proceedings of the Royal Society A: Mathematical, Physical and Engineering Sciences*, Vol. 467, No. 2125, 2011, pp. 144–165.
<https://doi.org/10.1098/rspa.2010.0172>

P. G. Tucker
 Associate Editor